Three-dimensional crustal structure of the southern Sierra Nevada from seismic fan profiles and gravity modeling

Moritz M. Fliedner Department of Geophysics, Stanford University, Stanford, California 94305-2215
Stanley Ruppert Lawrence Livermore National Laboratory, Livermore, California 94550
Southern Sierra Nevada Continental Dynamics Working Group*

ABSTRACT

Traveltime data from the 1993 Southern Sierra Nevada Continental Dynamics seismic refraction experiment reveal low crustal velocities in the southern Sierra Nevada and Basin and Range province of California (6.0 to 6.6 km/s), as well as low upper mantle velocities (7.6 to 7.8 km/s). The crust thickens from southeast to northwest along the axis of the Sierra Nevada from 27 km in the Mojave Desert to 43 km near Fresno, California. A crustal welt is present beneath the Sierra Nevada, but the deepest Moho is found under the western slopes, not beneath the highest topography. A density model directly derived from the crustal velocity model but with constant mantle density satisfies the pronounced negative Bouguer anomaly associated with the Sierra Nevada, but shows large discrepancies of >50 mgal in the Great Valley and in the Basin and Range province. Matching the observed gravity with anomalies in the crust alone is not possible with geologically reasonable densities; we require a contribution from the upper mantle, either by lateral density variations or by a thinning of the lithosphere under the Sierra Nevada and the Basin and Range province. Such a model is consistent with the interpretation that the uplift of the present Sierra Nevada is caused and dynamically supported by asthenospheric upwelling or lithospheric thinning under the Basin and Range province and eastern Sierra Nevada.

INTRODUCTION

The deep crustal structure of the Sierra Nevada batholith has been controversial because of contradictory results from seismic studies. Two end-member models have been proposed: a thick Airy-isostatic mountain root (Eaton, 1966), or a thin crust (Carder, 1973) overlying an anomalous mantle that provides isostatic compensation. The time difference between Mesozoic batholith formation (Bateman and Eaton, 1967) and Cenozoic uplift (Huber, 1981) is difficult to reconcile with Airy-root compensation, unless one invokes a mechanism of overcompensation prior to uplift, such as Chase and Wallace's (1988) flexural support by a strong lithosphere that allowed local equilibrium only after breaking by Basin and Range extensional faulting. Alternatively, Crough and Thompson (1977) attributed the forces driving Cenozoic uplift to thermal thinning of the lithosphere that replaced cold, dense subducting oceanic lithosphere with hot, buoyant asthenospheric mantle. The latter model does not require a crustal root to balance the Sierra Nevada and is supported by heat-flow data from the southern Sierra Nevada (Saltus and Lachenbruch, 1991).

Our seismic refraction survey in the Southern Sierra Nevada Continental Dynamics (SSCD) project was designed to resolve the controversy around the crustal structure of the Sierra Nevada (Park et al., 1995; Wernicke et al., 1995). The survey consisted of two crossing lines, with a shot spacing of about 50 km and a maximum shot-receiver offset of 330 km in the north-south line and 390 km in the west-east line (Fig. 1). Nineteen shots were recorded as conventional in-line shots. However, in an effort to address better a three-dimensional problem, four shots were fired in a fan geometry as well: shotpoints (SP) 3 and 4 of the west-east line were reused and recorded in the north-south line and SP 12 and 13 of the north-south line were reused and recorded in the west-east line. Seismic waves from a fan shot (off-line shot) fan across, or sweep out, large parts of the crust in the zone between the receiver line and the shot, thus allowing three-dimensional (3-D) analyses of structure and velocity. A modified west-east line later recorded the NPE (Non-Proliferation Experiment) 1 kiloton explosion at the Nevada Test Site as a fan shot (Fig. 1).

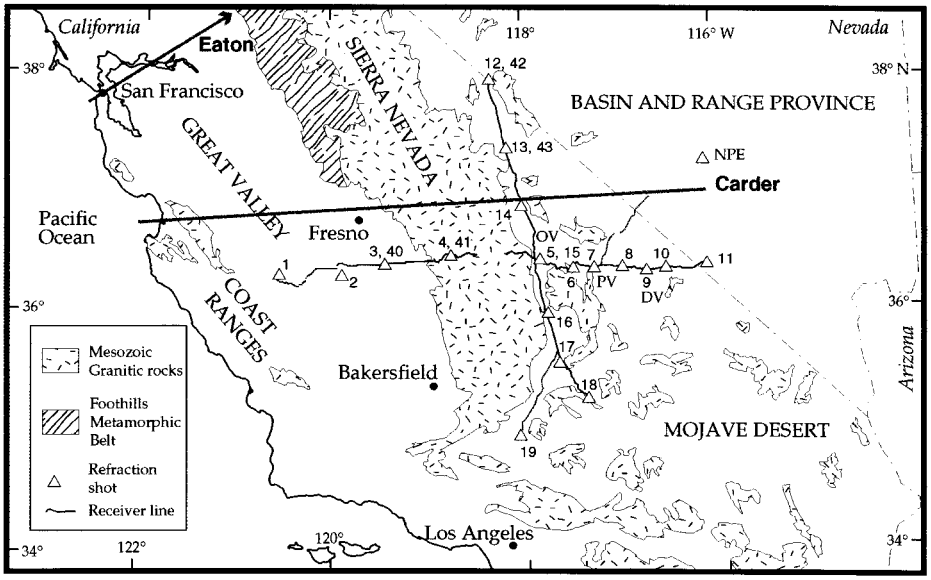

Figure 1. Location of Southern Sierra Nevada Continental Dynamics seismic refraction lines. Shots 1 to 19 were recorded in line. Shots 40 to 43 are fan shots: 40 and 41 recorded in north-south receiver line, 42 and 43 in west-east line. NPE is Non-Proliferation-Experiment shot fired at Nevada Test Site and recorded in west-east line (between SP 1 and 7) and short line from SP 7 toward NPE. OV is Owens Valley, PV is Panamint Valley, and DV is Death Valley. Thick lines locate profiles (Eaton, 1966; Carder, 1973) shown in Figure 2C.

*P. E. Malin (Duke University), S. K. Park (University of California at Riverside), G. Jiracek (San Diego State University), R. A. Phinney (Princeton University), J. B. Saleeby, B. Wernicke, R. Clayton (California Institute of Technology), R. Keller, K. Miller (University of Texas, El Paso), C. Jones (University of Nevada, Reno), J. H. Luetgert, W. D. Mooney, H. Oliver (U.S. Geological Survey), S. L. Klemperer, G. A. Thompson (Stanford University).

Data Repository item 9620 contains additional material related to this article.

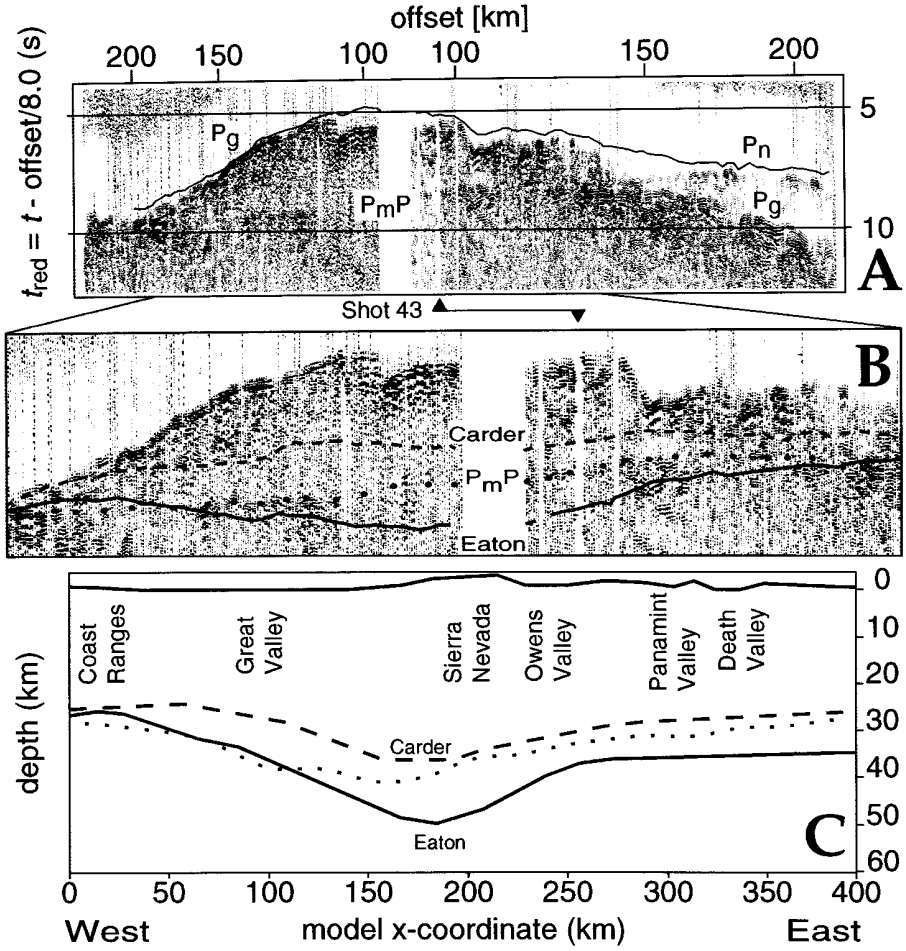

Figure 2. A: Receiver gather of fan shot 43; trace number (west-east coordinate) is plotted against reduced traveltime t_{red}. Shotpoint (triangle) was 95 km north of receiver line. Offset is shot-receiver distance. Traces are amplitude-squared, filtered from 2 to 20 Hz and have 7 s automatic gain control applied. Traces are equally spaced, leading to nonlinear offset scale (abscissa). Solid line is modeled first arrival (predicted times seem to precede observed times, because first arrival is weak or emergent for most of profile and is therefore not visible at this scale; actual root mean square misfit between modeled and observed traveltimes is only 80 ms for this shotpoint). B: Enlargement of A, with picks of P_mP used in this study (dots) compared with calculated traveltimes for two end-member seismic models of Sierra Nevada root: Eaton (deep root, solid line) and Carder (shallow, low-relief Moho, dashed line). C: Cross-sectional cartoon of Carder model (dashed line), Eaton model (solid line), and our final model (dotted line).

SSCD PROFILES—AVAILABLE DATA AND 3-D ANALYSIS

As an example of the fan recordings, the receiver gather from fan shot 43 (Fig. 2A) shows clear crustal (P_g) and mantle (P_n) refractions and Moho reflections (P_mP). (See Appendix 1[1] for more shot gathers.) We compare these data with traveltimes calculated for the actual recording geometry from a priori two-dimensional models extended into the third dimension representing two end-member crustal models of the Sierra Nevada. "Eaton" stands for the Airy-root model following Eaton (1966), and "Carder" for the nearly rootless model following Carder (1973) (Fig. 2C; for location of Eaton and Carder data, see Fig. 1).

Our 3-D interpretation used traveltime data from all the fan and in-line shots, including NPE. The velocities between the lines are less well constrained than directly under the lines because of the small number of fan recordings and the lack of short-offset information that is inherent in the fan geometry (the minimum offsets range from 72 km for SP 41 to 160 km for SP 42; ray coverage in Fig. 3A; data in Appendix 1 [see footnote 1]). Crustal velocities were determined by inverting P_g traveltimes, and although velocities of the lower crust are unconstrained by first arrivals, they are sampled by the secondary part of the P_g phase (beyond the P_n crossover point), albeit more sparsely than the upper crust. Using the crustal velocity model derived from the refracted arrivals, the P_mP reflection times determine the depth to the Moho. P_n arrivals constrain the upper mantle velocities directly beneath the Moho, and they were inverted after we modeled depth to Moho.

The inversion was done using a 3-D finite-difference traveltime modeling and inversion code (modified from Vidale, 1990; Hole, 1992; Hole and Zelt, 1995). Our starting model was one-dimensional, with a linear velocity-depth function. Each step of the iteration consists of traveltime calculation and ray tracing to account properly for position of the rays, and a nonlinear tomographic inversion that updates the velocity model according to the computed traveltime residuals. Because the velocity inversion is nonunique, especially in the off-line regions with sparse ray coverage, we used large smoothing filters on the calculated velocity perturbations in the beginning, and thereafter decreased the filter size gradually. This procedure biases the inversion in favor of large, smooth velocity anomalies; i.e., it should most reliably reveal the first-order features in the velocity structure.

Next, we used our velocities from the P_g inversion for the interpretation of the P_mP reflected arrivals to produce a model that includes a steplike velocity increase from lower crustal to mantle velocities across the Moho, necessary to produce the observed P_mP reflections. P_mP can be recognized clearly on most in-line shots, and then can be transferred to the fan profiles at the line ties to get consistent picks (Appendix 1, see footnote 1). Starting with a constant Moho depth of 30 km, we used a code by Hole and Zelt (1995) to calculate 3-D finite-difference reflection traveltimes and to derive depth perturbations from observed P_mP traveltime residuals. The depth perturbations were gridded to calculate the new Moho; this was iterated until the Moho surface did not change significantly. Finally, P_n arrivals were inverted for mantle velocities after the position of the Moho had been fixed.

Due to uncertainties in picking secondary arrivals consistently and the sparse occurrence of reflection points in three dimensions, the root-mean-square misfit in depth for the final Moho map (Fig. 3B) is 2.2 km. The final model has a root-mean-square misfit of 120 ms (for comparison, in the areas of steepest topography, the elevation difference between *adjacent* receivers corresponds to a relative static shift of about 200 ms); varying the velocities in the constrained parts of the model by more than 0.2 km/s degrades the fit significantly, and we estimate the depth error for our Moho map, including velocity uncertainties, to be ±3 km. (See Appendix 2 [footnote 1] for resolution and error tests for our inversion

[1]Data Repository item 9620, Appendices 1 and 2, is available on request from Documents Secretary, GSA, P.O. Box 9140, Boulder, CO 80301.

Figure 3. A: Map view of first-arrival ray coverage from all shots. Map covers same area as B. B: Contours of Moho depth beneath sea level superimposed on Sierra Nevada batholith. Purple line on east side is crest line. Large dots are reflection points that constrain Moho relief. Red dots are receivers; blue triangles are shotpoints used for interface inversion. Dotted line between shotpoint 1 and X is location of section shown in C. C: Vertical cross section (SP 1 to X in A and B) through velocity model approximately perpendicular to strike of Sierra Nevada. Velocity contour lines (in km/s) and outline of local topography are superimposed on projection of first-arrival ray coverage in 80-km-wide swath centered on section. Interpreted Moho coincides with 7.6 km/s contour.

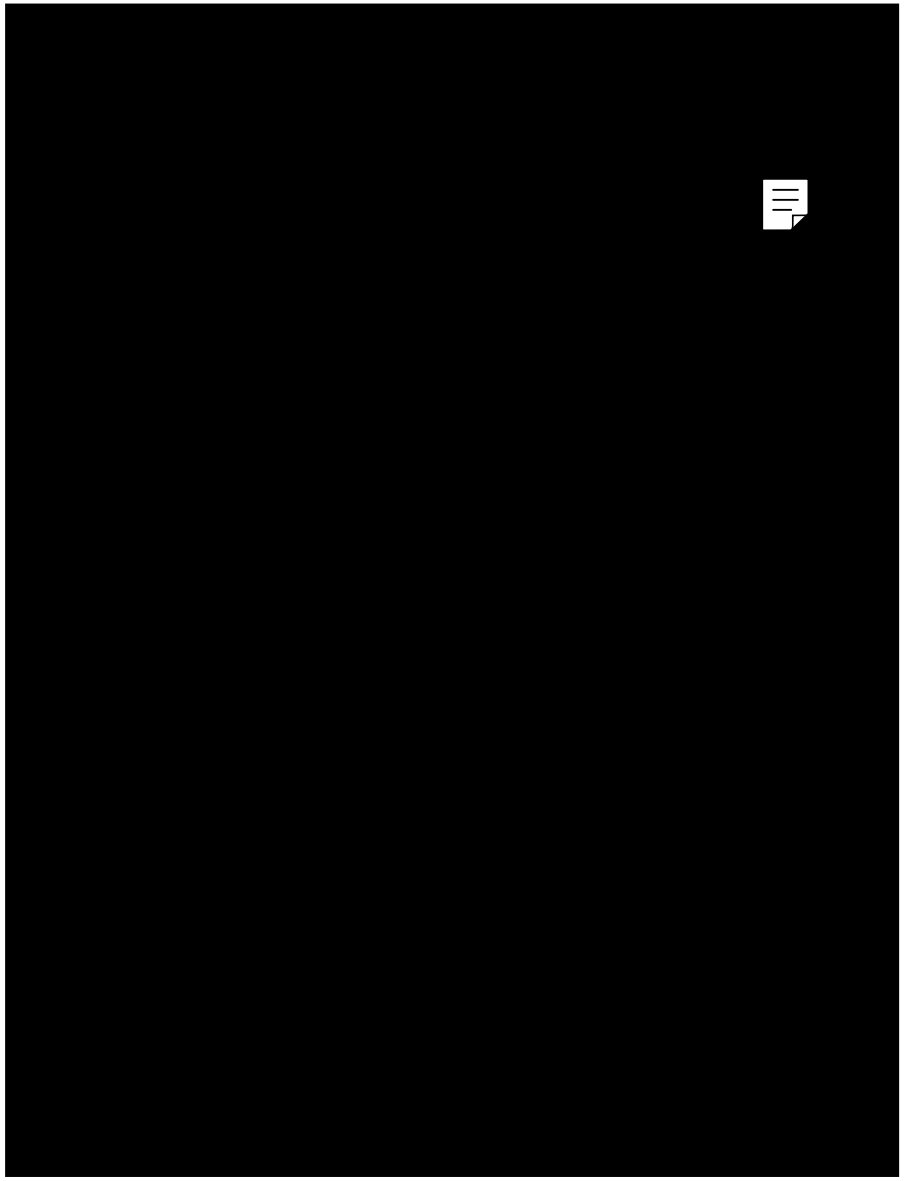

Figure 4. Observed (squares) and modeled (solid line) gravity (Δg) for two-dimensional profile along west-east refraction line. Modeled gravity is referenced to mid-ocean-ridge lithosphere (Lachenbruch and Morgan, 1990). Model topography from Diment and Urban (1981). A: Crustal densities are from velocity-density curve ($V \propto \rho$); mantle density is constant 3280 kg/m^3. B: Crustal densities in Sierra Nevada as in A; density of Great Valley basement is $\geq$2950 kg/m^3, and densities in Basin and Range are $\leq$2750 kg/m^3. C: Crustal densities as in A, but thickness of lithosphere (effective mantle density) varies.

methods, including checkerboard tests for the SSCD aquisition geometry, and further technical details of the modeling.)

RESULTS FROM VELOCITY INVERSION AND MOHO DEPTH MODELING

The most important velocity gradient in our model is the transition from crustal P velocities to P_n velocities of about 7.8 km/s across the Moho. Crustal velocities are lowest in the Sierra Nevada and parts of the Basin and Range province, and high in the Great Valley (Fig. 3C). The Moho (Fig. 3B) deepens northward from around 28 km at the southern end of the Sierra Nevada to 43 km east of Fresno. Figure 3C shows an arbitrary cross section (dotted line in Fig. 3B) through our final 3-D velocity model, chosen as a dip line across the Sierra Nevada through the region of deepest Moho. We mapped a closed contour of 43 km west of shotpoint 14, and the crust thins in the north of our study area. The thickest Sierra Nevada crust is therefore offset 40 km to the west with respect to the crest of the mountain range. Only 20 km east of the highest topography (crestline in Fig. 3B), the crust is as thin as 30–35 km under the north-south line. The thickened crust in the western Sierra Nevada cannot therefore be called a "root" in the sense of local Airy-isostatic compensation. P_mP reflections from the west-east line show Moho depths from 30 to 34 km under the Basin and Range province and 34 to 42 km in the Sierra Nevada; the maximum depth is under the western slopes, and the depth decreases under the Great Valley toward the Coast Ranges to less than 30 km. The crustal thicknesses for the Basin and Range are consistent with other surveys (see Jones, 1987, for a compilation). The Moho depth under the Great Valley is poorly constrained by our data (P_mP arrivals from SP 1 only), but our results are consistent with previous studies (e.g., Holbrook and Mooney, 1987).

IMPLICATIONS FROM COMPARISON WITH GRAVITY

Because the crustal root is offset westward with respect to the High Sierra, it fails to explain the location of the 75 mgal Bouguer gravity trough associated with the Sierra Nevada. Furthermore, the regional gravity difference of 75 mgal between the Basin and Range and the Great Valley (Fig. 4) exists despite similar crustal thicknesses in these regions. The magnitude of the Sierra Nevada gravity low can be roughly modeled using a linear relation between crustal velocities and densities (Oliver, 1977; Thompson and Talwani, 1964; Fig. 4A), and a mantle of constant density (3280 kg/m^3) for a profile along the west-east refraction line (Fig. 4A). We hold the model at the west end at 0 mgal in isostatic equilibrium with the mid-ocean-ridge model described by Lachenbruch and Morgan (1990). This leaves a 50 mgal deficit in modeled gravity for the Great Valley, and a 100 mgal surplus for the Basin and Range. To fit the observed gravity, we consider two extreme possibilities: compensating the residual by crustal anomalies alone (Fig. 4B), or compensating the residual by upper mantle anomalies alone (Fig. 4C). The model shown in Figure 4B achieves a satisfactory fit by assuming the following density anomalies in the Great Valley and Basin and Range crust: 2950 kg/m^3 for the entire basement of the Great Valley (depth range of 5 km to Moho), a density appropriate for the Great Valley ophiolite and mafic basement (Griscom and Jachens, 1990), and a maximum density of 2750 kg m^{-3} for the Basin and Range crust to the east of Owens Valley. The attempt to fit the observed gravity with anomalies in the mantle alone is more difficult, because of the steep gravity gradient between the Great Valley and the Sierra Nevada. In the model shown in Figure 4C, we vary the depth to the asthenosphere by as much as 70 km to achieve the necessary lateral variation in mantle density. Although the anomalous densities in the model in Figure 4B are not unusual for crustal rocks, they deviate considerably from the average crustal density of 2830 kg/m^3 (Christensen and Mooney, 1995) if used for the entire crust. It is furthermore unlikely that the lower crust in the Basin and Range has velocities >6.5 km/s, but densities corresponding to those of felsic rocks. We therefore prefer at least some gravity contribution from an anomalous upper mantle: low velocity, high density under the western Sierra Nevada (possibly eclogite derived from conversion of gabbroic arc crust; Wernicke et al., 1995), or low density under the eastern Sierra and western Basin and Range due to asthenospheric upwelling (Crough and Thompson, 1977).

CONCLUSIONS

The southern Sierra Nevada batholith has a minor crustal thickening with Moho depth no greater than 43 ± 3 km. This crustal welt is laterally displaced west of the highest topography, and it is insufficient to explain the Sierra Nevada gravity low, which therefore requires laterally varying mantle densities.

ACKNOWLEDGMENTS

The Southern Sierra Continental Dynamics project is supported by the National Science Foundation (NSF) grant EAR-91-19263 to Duke University; this work was supported by NSF grants EAR-92-04998 and EAR-94-05577 to Stanford University and Department of Energy contract W-7405-ENG-48 to Lawrence Livermore National Laboratory. The seismic data were collected with support from the U.S. Geological Survey and the Program for Array Seismic Studies of the Continental Lithosphere (PASSCAL) and are available from the Incorporated Research Institutions for Seismology (IRIS) Data Management Center, via http://www.iris.washington.edu/. We thank Tom Parsons and an anonymous reviewer for helpful reviews.

REFERENCES CITED

Bateman, P. C., and Eaton, J. P., 1967, Sierra Nevada batholith: Science, v. 158, p. 1407–1417.

Carder, D. S., 1973, Trans-California seismic profile, Death Valley to Monterey Bay: Seismological Society of America Bulletin, v. 63, p. 571–586.

Chase, C. G., and Wallace, T. C., 1988, Flexural isostasy and uplift of the Sierra Nevada of California: Journal of Geophysical Research, v. 93, p. 2795–2802.

Christensen, N. I., and Mooney, W. D., 1995, Seismic velocity structure and composition of the continental crust: A global view: Journal of Geophysical Research, v. 100, p. 9761–9788.

Crough, S. T., and Thompson, G. A., 1977, Upper mantle origin of Sierra Nevada uplift: Geology, v. 5, p. 396–399.

Diment, W. H., and Urban, T. C., 1981, Average elevation map of the conterminous United States (Gilluly averaging method): U.S. Geological Survey Geophysical Investigations Map GP-933, scale 1:2 500 000.

Eaton, J. P., 1966, Crustal structure in northern and central California from seismic evidence, *in* Geology of northern California: California Division of Mines and Geology Bulletin, v. 190, p. 419–426.

Griscom, A., and Jachens, R. C., 1990, Tectonic implications of gravity and magnetic models along east-west seismic profiles across the Great Valley near Coalinga, *in* Rymer, M. J., and Ellsworth, W. L., eds., The Coalinga, California, earthquake of May 2, 1983: U.S. Geological Survey Professional Paper 1487, p. 69–78.

Holbrook, W. S., and Mooney, W. D., 1987, The crustal structure of the axis of the Great Valley, California, from seismic refraction measurements: Tectonophysics, v. 140, p. 49–63.

Hole, J. A., 1992, Nonlinear high-resolution three-dimensional seismic travel time tomography: Journal of Geophysical Research, v. 97, p. 6553–6562.

Hole, J. A., and Zelt, B. C., 1995, 3-D finite-difference reflection traveltimes: Geophysical Journal International, v. 121, p. 427–434.

Huber, N. K., 1981, Amount and timing of late Cenozoic uplift and tilt of the central Sierra Nevada, California—Evidence from the upper San Joaquin River basin: U.S. Geological Survey Professional Paper 1197, 28 p.

Jones, C. H., 1987, Is extension in Death Valley accommodated by thinning of the mantle lithosphere beneath the Sierra Nevada, California?: Tectonics, v. 6, p. 449–473.

Lachenbruch, A. H., and Morgan, P., 1990, Continental extension, magmatism and elevation; formal relations and rules of thumb: Tectonophysics, v. 174, p. 39–62.

Oliver, H. W., 1977, Gravity and magnetic investigations of the Sierra Nevada batholith, California: Geological Society of America Bulletin, v. 88, p. 445–461.

Park, S. K., Clayton, R., Ducea, M., Jones, C. H., Ruppert, S., and Wernicke, B., 1995, Project combines seismic and magnetotelluric surveying to address the Sierran root question: Eos (Transactions, American Geophysical Union), v. 76, p. 297–298.

Saltus, R. W., and Lachenbruch, A. H., 1991, Thermal evolution of the Sierra Nevada: Tectonic implications of new heat flow data: Tectonics, v. 10, p. 325–344.

Thompson, G. A., and Talwani, M., 1964, Crustal structure from Pacific basin to central Nevada: Journal of Geophysical Research, v. 69, p. 4813–4837.

Vidale, J. E., 1990, Finite-difference calculation of traveltimes in three dimensions: Geophysics, v. 55, p. 521–526.

Wernicke, B., and 18 others, 1995, Origin of high mountains in the continents: The southern Sierra Nevada: Science, v. 270.

Manuscript received August 21, 1995
Revised manuscript received December 21, 1995
Manuscript accepted December 22, 1995

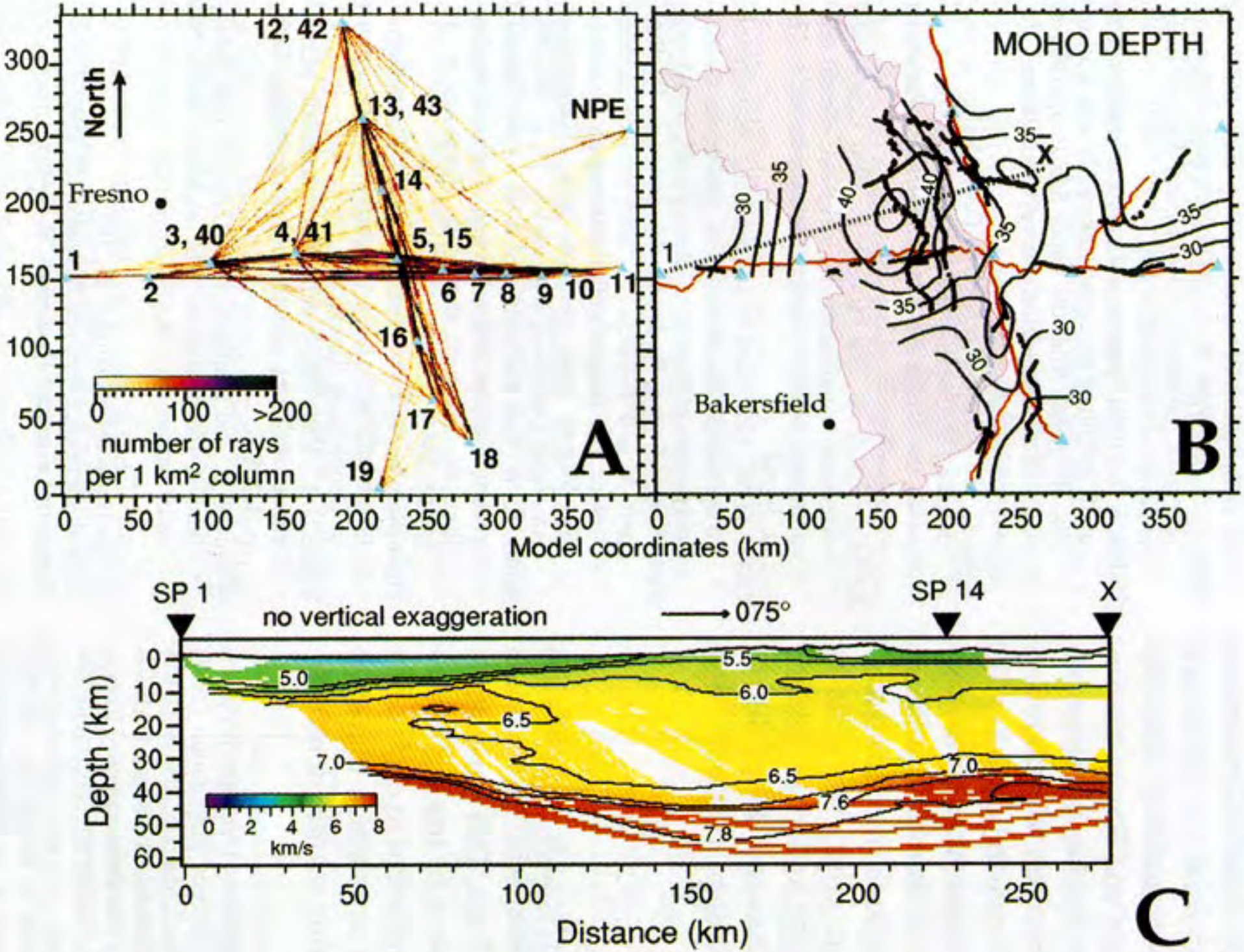
North
Fresno
12, 42
13, 43
NPE
14
3, 40
4, 41
5, 15
1
2
6 7 8 9 10 11
16
17
18
19
0 100 >200
number of rays
per 1 km² column
A
MOHO DEPTH
Bakersfield
X
B
Model coordinates (km)
SP 1
SP 14
X
no vertical exaggeration
075°
Depth (km)
km/s
Distance (km)
C

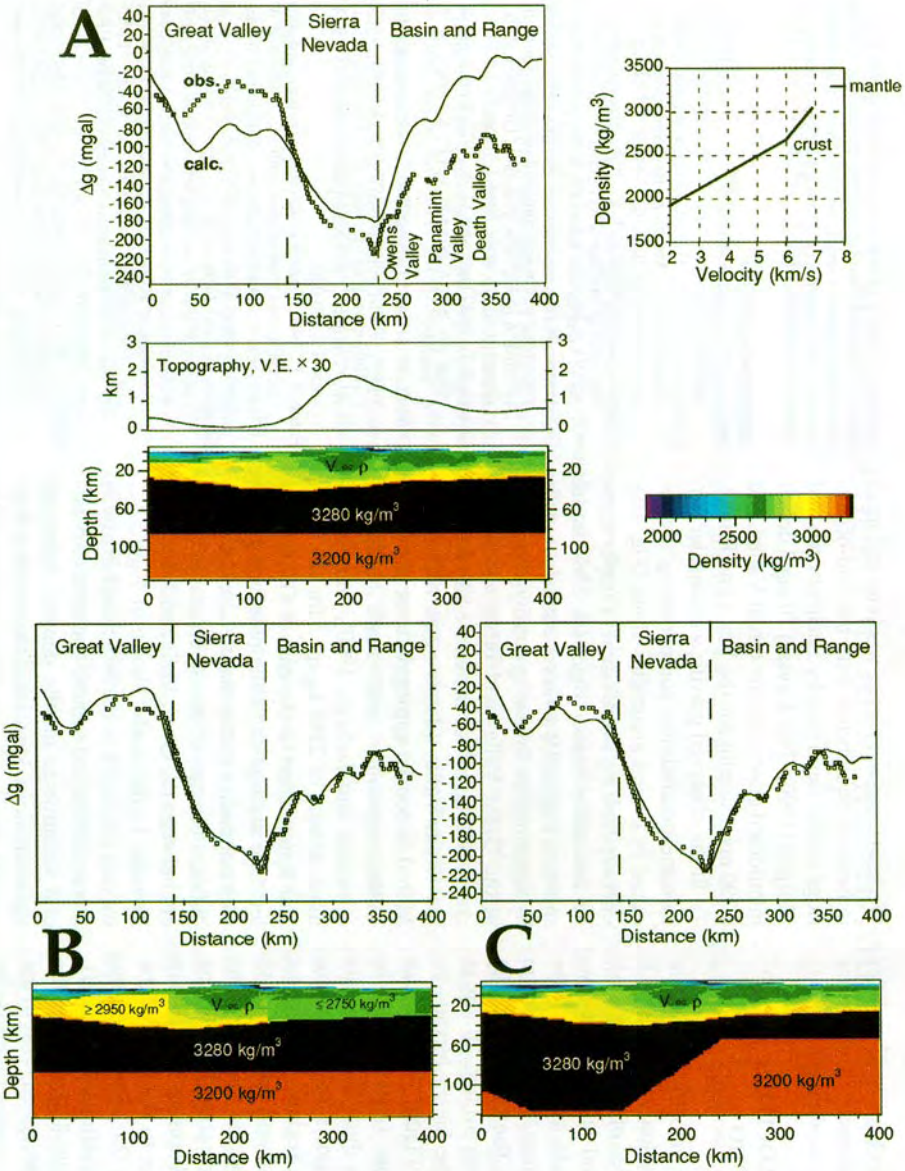
A
Great Valley
Sierra Nevada
Basin and Range
obs.
calc.
Δg (mgal)
Owens Valley
Panamint Valley
Death Valley
Distance (km)
Density (kg/m3)
Velocity (km/s)
mantle
crust
Topography, V.E. × 30
km
Depth (km)
V ∞ ρ
3280 kg/m3
3200 kg/m3
Density (kg/m3)
B
C
≥ 2950 kg/m3
≤ 2750 kg/m3

Supplementary Material

Appendix 1: **Shot gathers**

In this appendix we show gathers of the four fan-shots and their accompanying in-line shots (figs. A1-1 to A1-4). All gathers have constant trace spacing (non-linear offset scale) and travel-times are reduced at 8.0 km s^{-1}. The traces are bandpass filtered 2-20 Hz and equalised. The modelled (**not** picked) travel-times of P_g, P_n, and P_mP from the final model (figs. 3b, 3c) have been overlain *only* where travel-time picks were made and used in our inversions. The gathers of the north-south line (SPs 40, 41, 12, and 13) show the receiver-line segment between SP 12 and 18, and do not show the segment between SP 17 and 19. For shotpoint locations, see Fig. 1. On each figure the line intersection is marked at the point where the north-south and west-east lines cross. At this point the records from the paired fan and in-line shots fired in the same location (e.g. shots 40 and 3) should be identical, and phases that are easily identifiable as P_g, P_n, or P_mP on the in-line profiles from their characteristic velocity can be transferred to the fan profiles.

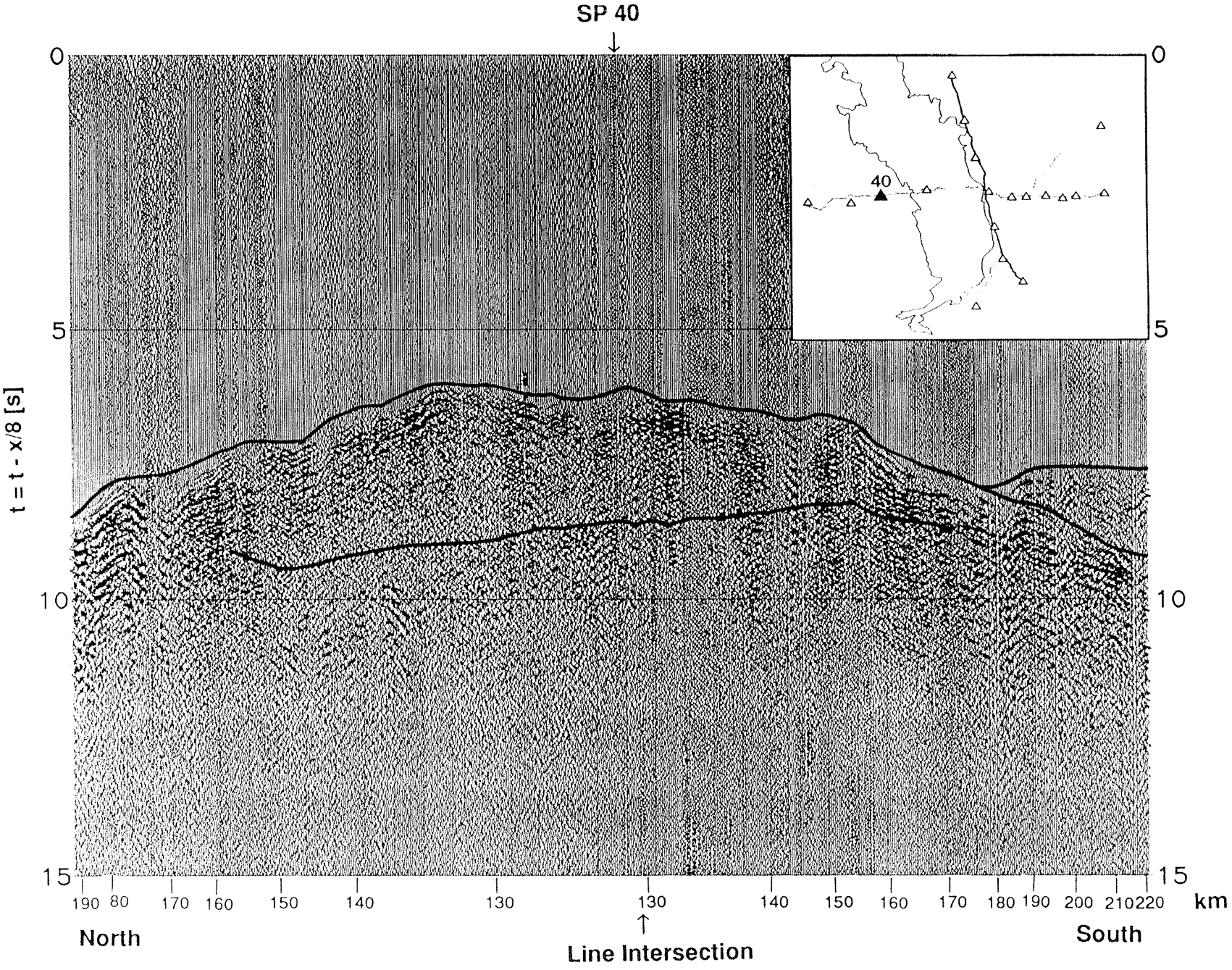

A1-1a shotpoint 40 (fan)

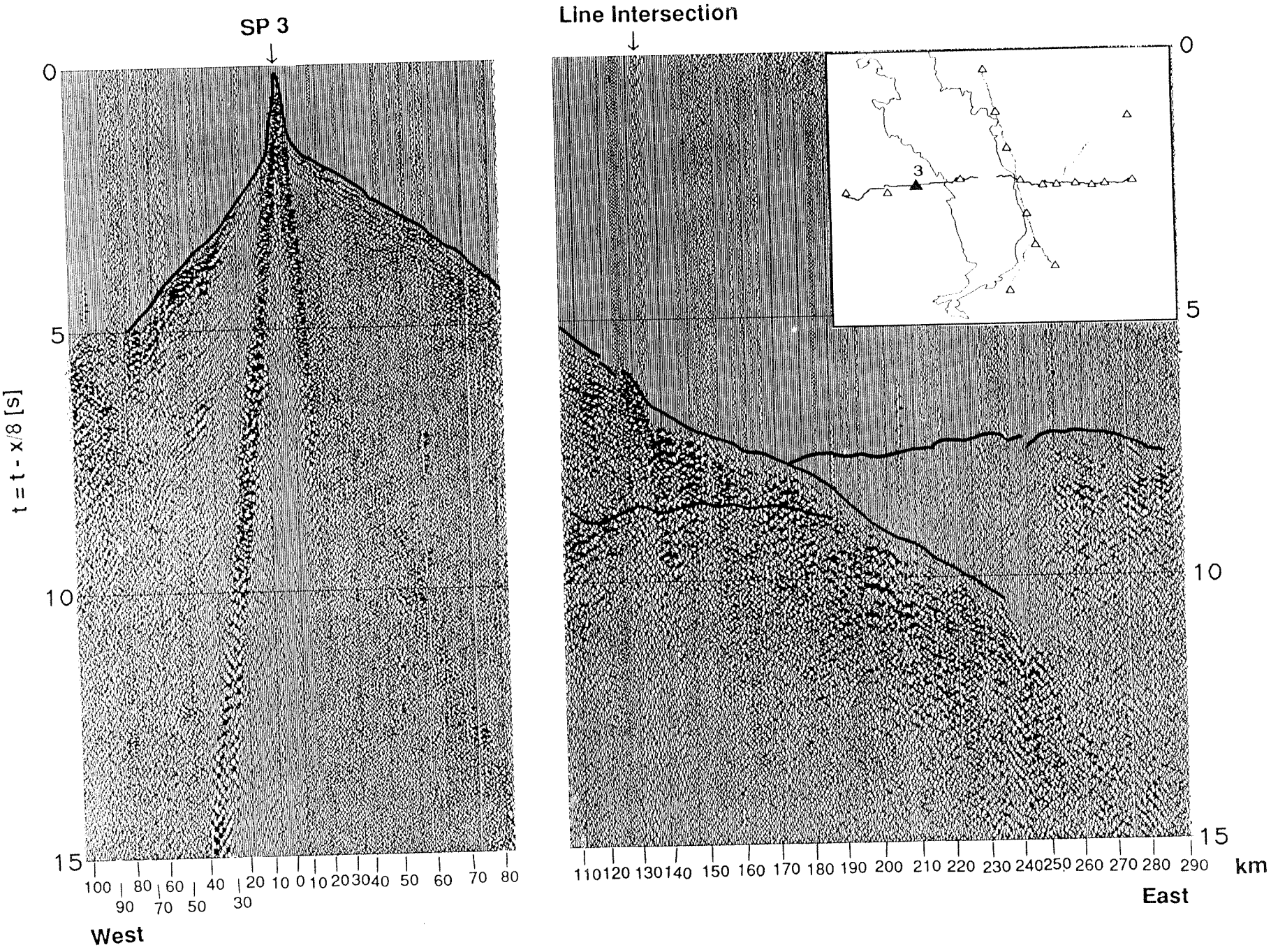

A1-1b shotpoint 3 (in-line)

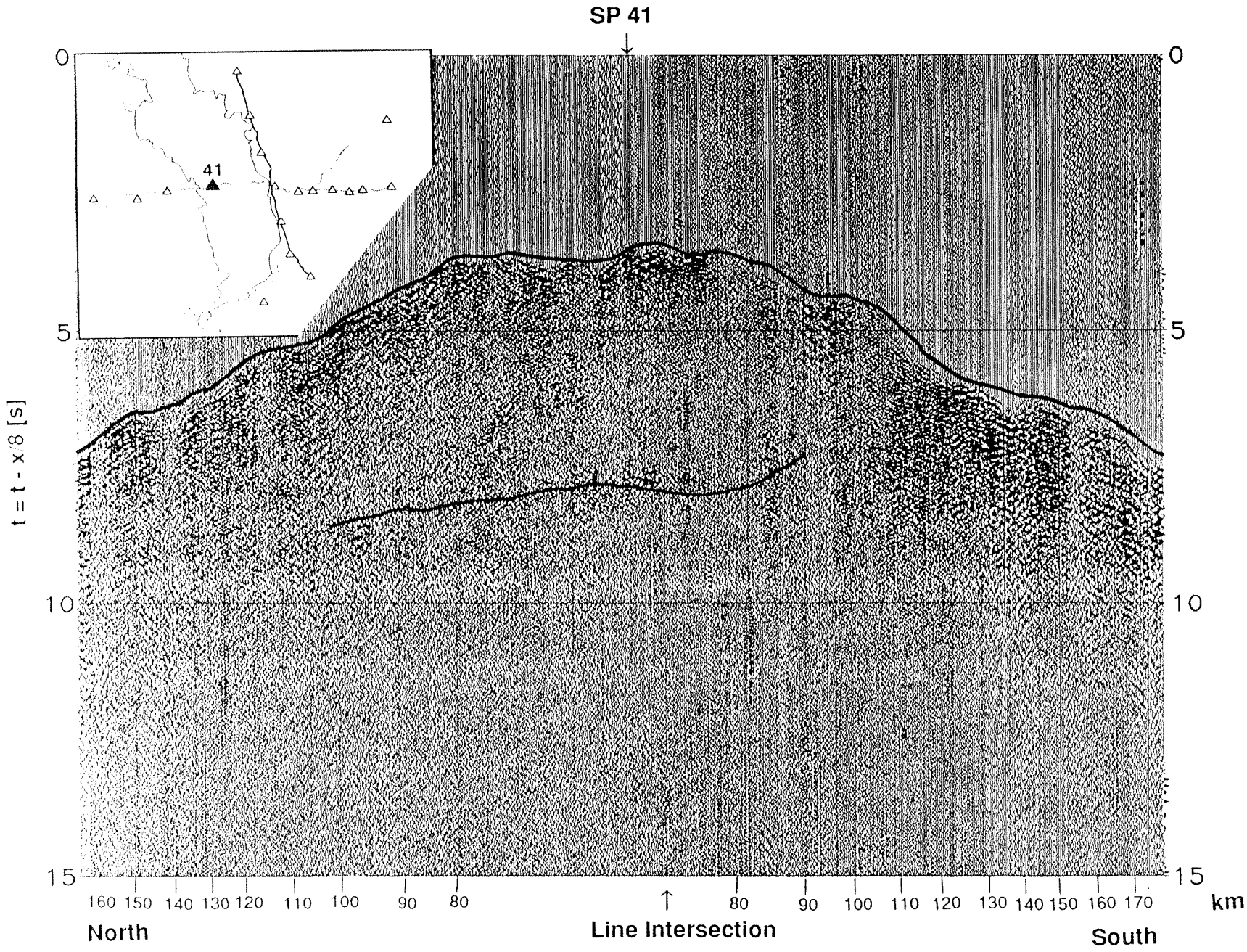

A1-2a shotpoint 41 (fan)

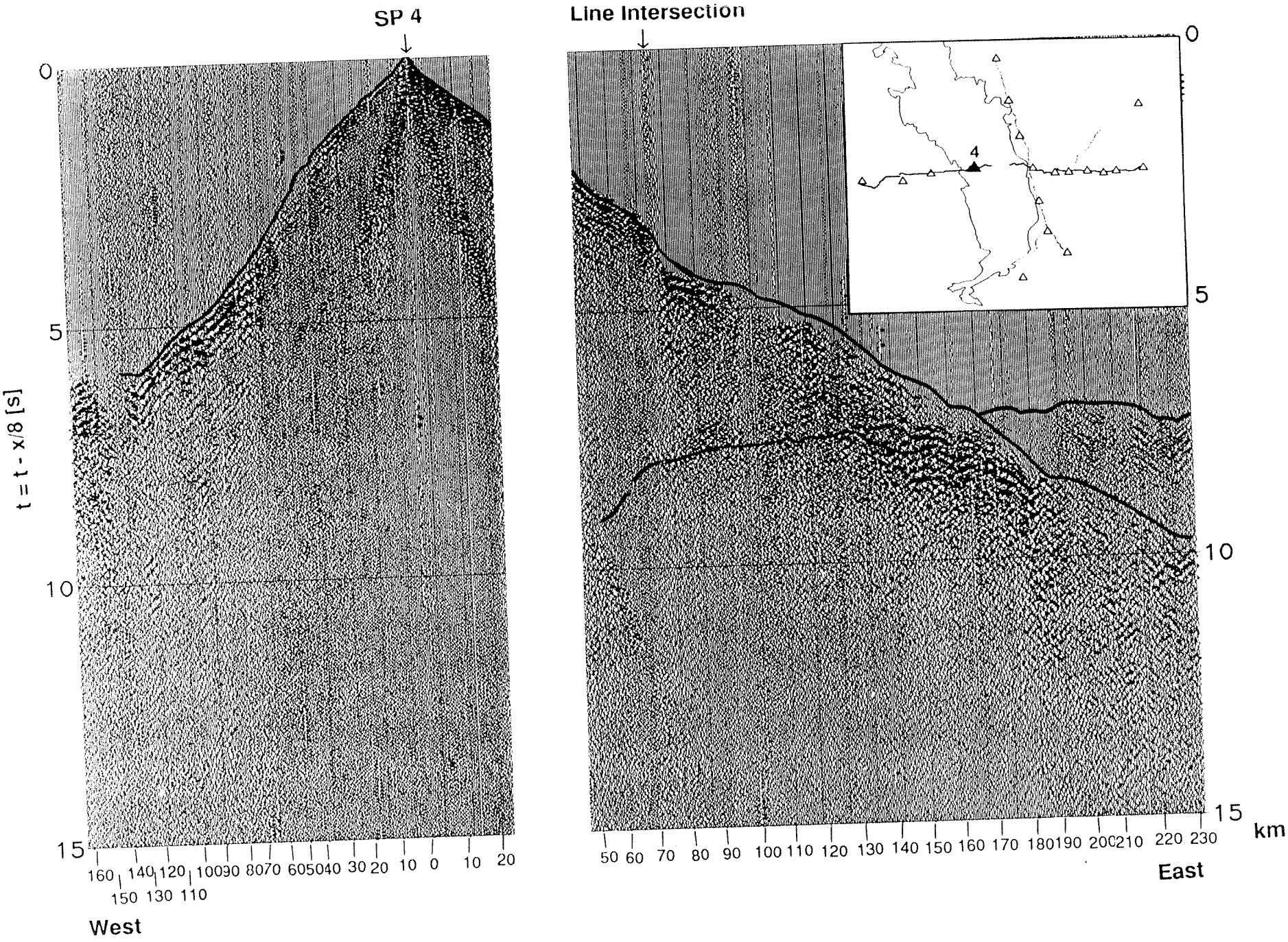

A1-2b shotpoint 4 (in-line)

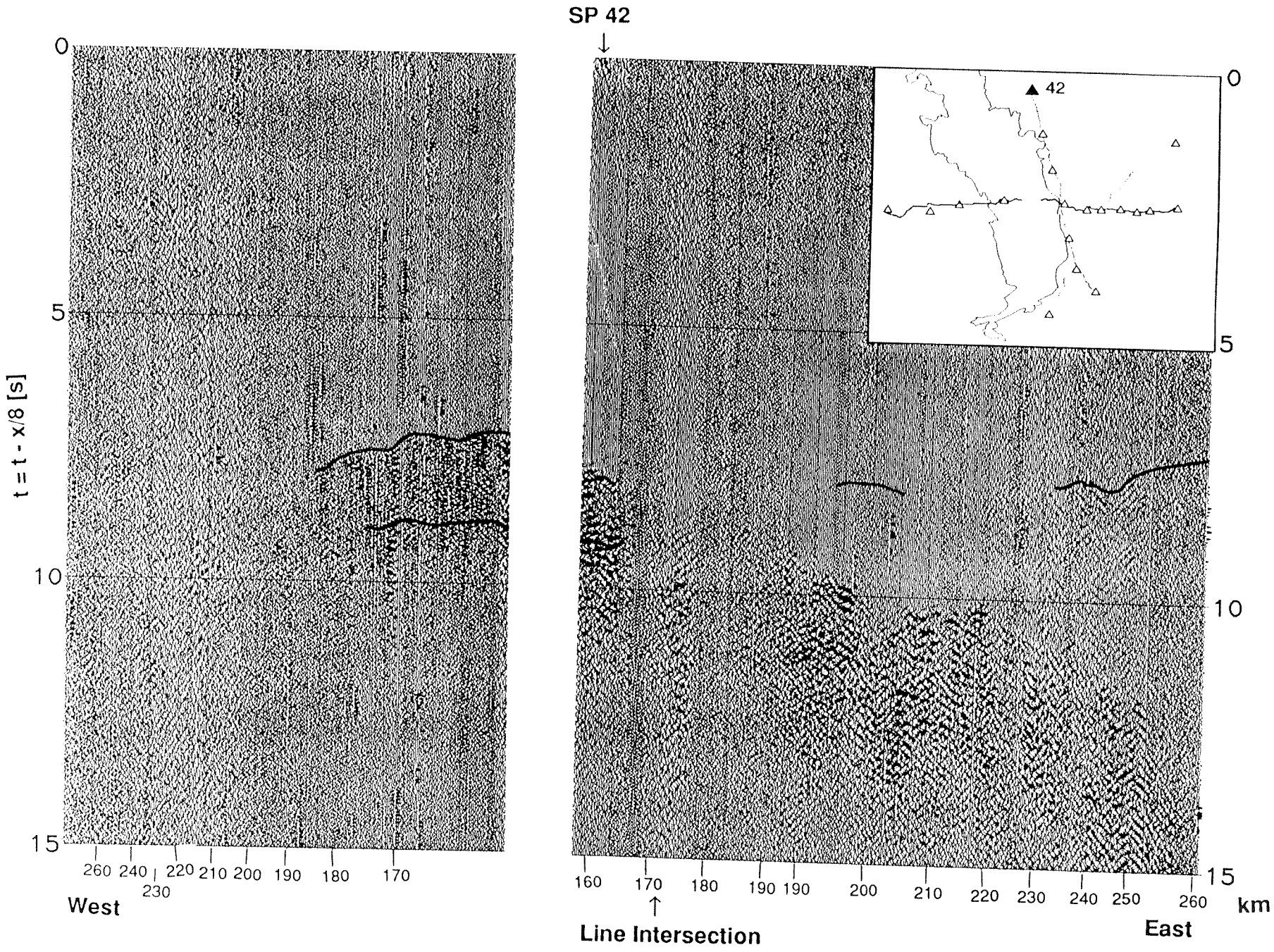

A1-3a shotpoint 42 (fan)

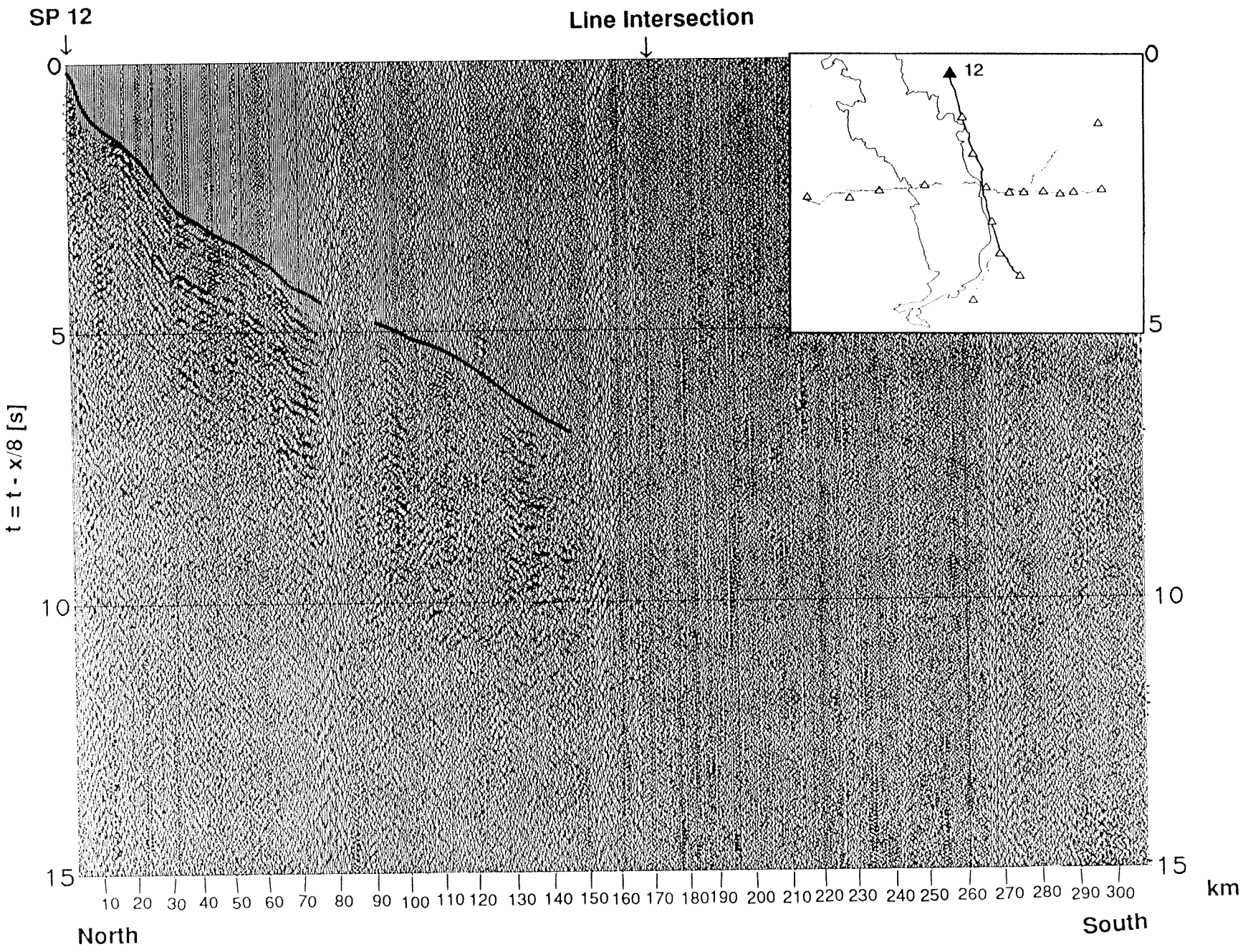

A1-3b shotpoint 12 (in-line)

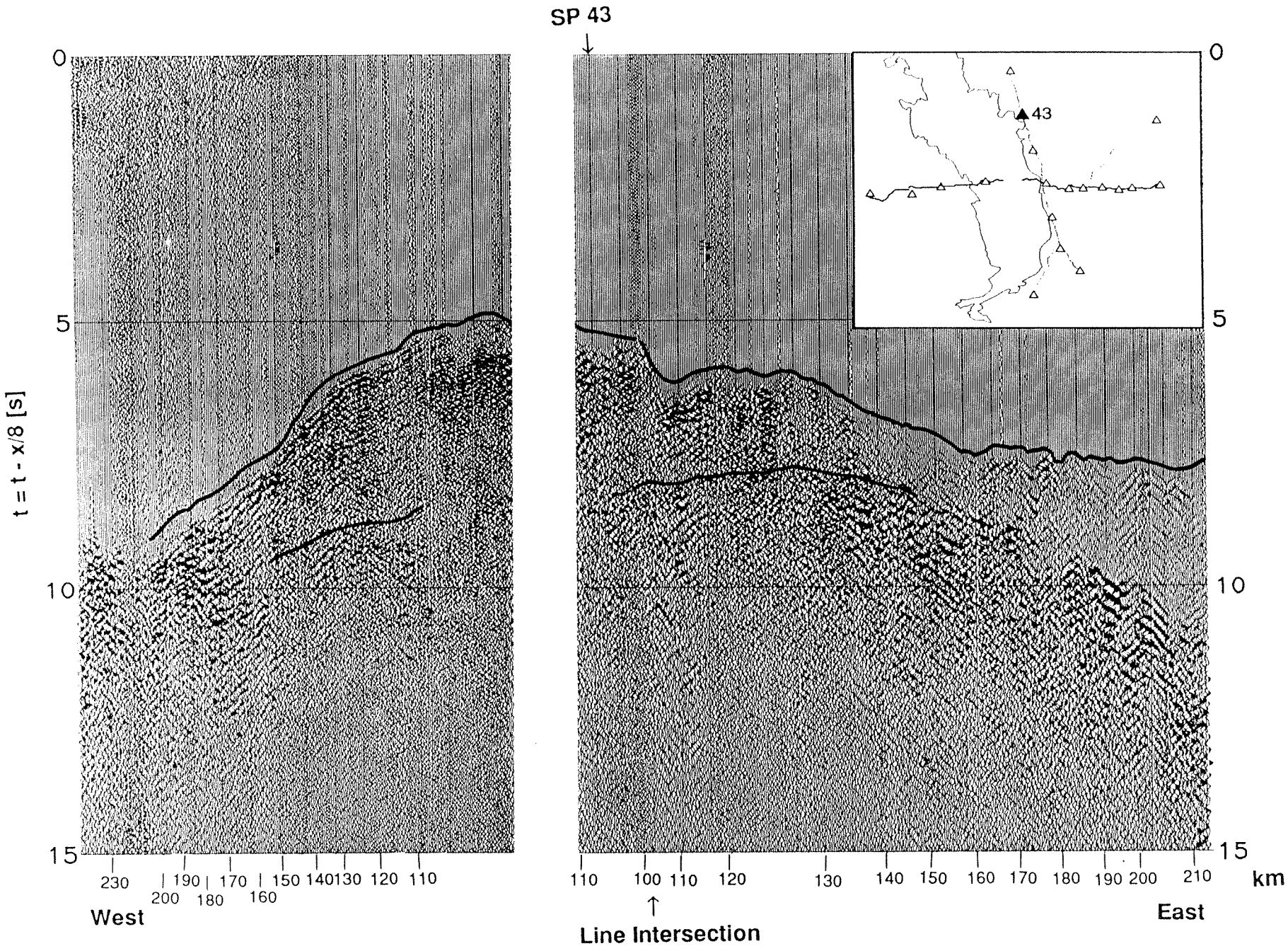

A1-4a shotpoint 43 (fan) (equivalent to fig. 2a)

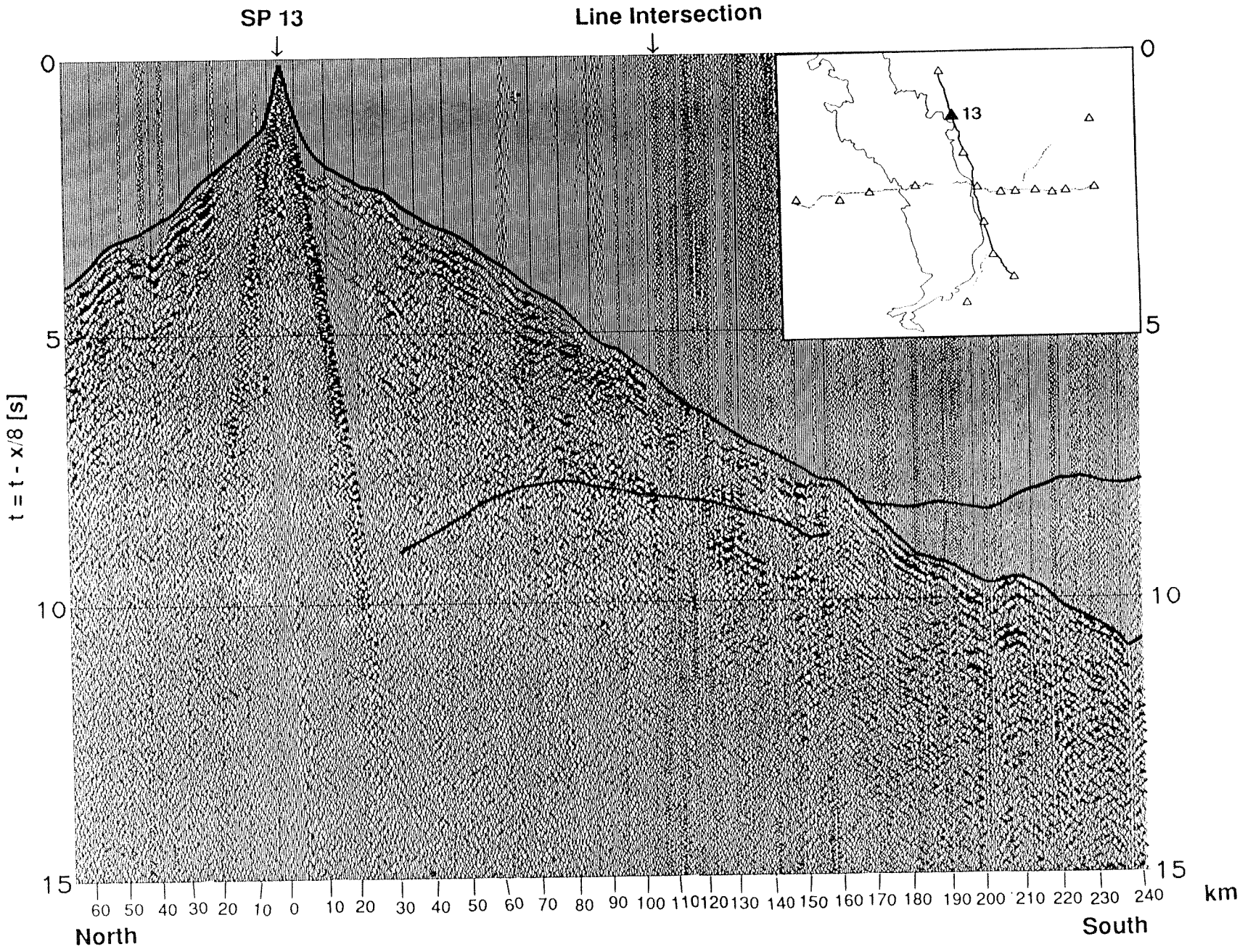

A1-4b shotpoint 13 (in-line)

Appendix 2: **Travel-time inversion methodology and tests of resolution**

Modelling methodology

We used travel-time picks of P_g, P_n, and P_mP phases to invert for the 3-D velocity structure (from the refracted arrivals) and the depth to the Moho interface (from the P_mP reflection). The inversion was done using a 3-D finite-difference travel-time modelling code (modified from *Vidale*, 1990; *Hole and Zelt*, 1995) and an inversion scheme developed by *Hole* (1992). In order to keep the 3-D gridded data volumes for travel-times and velocities within acceptable limits while using a fine node spacing (1 km) to ensure the necessary accuracy of the modelled travel-times, we calculated the travel-times in appropriately restricted sub-volumes only. For receivers in the west-east line we used a volume restricted to the model-coordinate range $0 \leq X \leq 400$ km, $150 \leq Y \leq 335$ km, and $-6 \leq Z \leq 60$ km, and for the receivers in the north-south line $95 \leq X \leq 285$ km, $0 \leq Y \leq 335$ km, and $-6 \leq Z \leq 60$ km (map, fig. 3a). In the inversion step, rays were traced from the receivers through the travel-time volume back to the shot, and velocity perturbations are calculated from the travel-time differences between model and observations and applied to the velocity model (*Hole*, 1992) consecutively for both receiver lines; inconsistencies between the two submodels were eliminated by averaging in the region of overlap. The updated velocity model then serves as input for the next modelling-inversion step.

The starting model was one-dimensional with a linear velocity-depth function (5.8 km s^{-1} at Z = -6 km, 8.0 km s^{-1} at Z = 30 km, 8.3 km s^{-1} at Z = 60 km). Since the velocity inversion is non-unique, especially in the off-line regions, which have only sparse ray coverage, we applied large smoothing filters (moving-average filters) to the calculated velocity perturbations in the first iterations, and thereafter decreased the filter size gradually. Table A2-1 summarises the smoothing filter sizes and the progress of the inversion. We changed the filter size according to subjective criteria, typically when the convergence rate (measured by the decrease in the global rms-misfit to the

observed travel-times per iteration for a specific filter) had slowed by an order of magnitude. This procedure biasses the inversion in favour of large, smooth velocity anomalies, i.e. it should most reliably reveal the first-order features in the velocity structure.

We next used the velocity model from the P_g arrivals for the following interpretation of the P_mP arrivals. Starting with a constant Moho depth of 30 km everywhere, we used a code by *Hole and Zelt* (1995) to calculate 3-D finite-difference reflection travel-times and to derive depth perturbations from observed P_mP travel-time residuals. The depth perturbations at each reflection point were then extrapolated by a combination of Laplacians and bicubic splines into a gridded Moho perturbation surface which was smoothed by a moving average filter of 50 km width in both horizontal directions (comparable to the shot spacing). The new Moho surface was used for the next travel-time modelling step and the whole process is iterated three times until the Moho surface stabilises. Finally, we inverted P_n for the mantle velocities beneath the fixed Moho.

The codes to compute our models (tomographic refraction inversion and reflecting-interface inversion) are freely available from John Hole, `hole@geo.stanford.edu` or `http://pangea.stanford.edu/~hole/home.html`.

Resolution of the models

Our major concerns in modelling the SSCD data were that our source and receiver geometry was adequate to construct the velocity and depth models in three dimensions (fig. A2-1), and that we should only interpret our model geologically where we had sufficient ray density (fig. A2-2).

A checkerboard test (fig. A2-1) was run to demonstrate the resolving power of the available P_mP ray coverage. Synthetic reflection travel-times were calculated in a 1-D velocity model with gradients similar to the modelled Sierra Nevada velocities and a 2-D sinusoidal reflector with 150 km wavelength and a peak-to-peak amplitude of

10 km (fig. A2-1a). Only shots and receivers of the SSCD profiles that were actually used for the real Moho depth model were used for the test. The starting model for the test inversion was a reflector of 35 km constant depth (average depth of the true reflector). Four iterations of the interface inversions were run; the reflection points plotted on the final output model (fig. A2-1b) are the reflection points calculated from the input model of this inversion step. The results of the third and fourth inversion do not differ greatly in the area constrained by reflection points: reflector highs and lows B, C, D, E, F, G, H and I that were hit by rays could be reconstructed within less than 700 m, and highs A and J could be partially reconstructed within 2 km. We used the same moothing parameters as for the real data inversion discussed in the main text. The rms-misfits we quote are the root mean square of the depth error between the synthetic and modelled Moho depths at the P_mP reflection points.

Data coverage

Figure A2-2 shows the ray coverage for P_g and P_n. P_g ray coverage is displayed in 10-km depth intervals to demonstrate which parts of the velocity model are directly constrained. The grayscale shows the ray-hit count per 1x1 km depth column (integrated over the 10 km depth interval, figs. A2-2a to d). P_n coverage is vertically integrated over the entire depth range beneath the Moho (fig. A2-2e). The vertical sections through the 3-D ray coverage volume along the and south-north (Y-), fig. A2-2f, west-east (X-), fig. A2-2g, axis show ray density integrated along the normal to the section. In the south-north section the integration range is restricted to $95 \leq X \leq 285$ km to have equal numbers of cells throughout the model, and in the west-east section the integration range is $150 \leq Y \leq 335$. To demonstrate the additional lower-crustal P_g ray-coverage provided by the fan shots, the last south-north section (fig. A2-2h; northern part of the model only) displays rays from just the three fan shots recorded in the west-east line (42, 43, and NPE) only.

Dependence of interface inversion on starting model

We ran several tests to show the robustness of the interface inversion. Again, only shots and receivers of the SSCD profiles that were actually used for the real Moho depth model (i.e., only observed P_mP reflections, figures A2-1 to 5) were used for the tests.

It can be shown that our interface inversion for Moho depth is independent of the starting model (for our final velocity model) (fig. A2-3). Starting from a flat reflector at 30 km (fig. A2-3a) and 45 km (fig. A2-3b) depth respectively, we ran each starting model through two iterations of the inversions without any additional constraints (apart from editing out any rays near grazing incidence that provide no meaningful depth information and are numerically unstable). We plot the difference between the two in figure A2-3c. The steep gradient towards a value of 15 km (difference between the starting models) in three corners of the model (fig. A2-3c) clearly delineates the area of constraint by reflection points and stable extrapolation (i.e. the area between and around the reflection points where the gridding algorithm produces the same Moho shape using identical gridding parameters for both starting models). For the shaded area, which is the region contoured in figure 3b, the rms-errors are less than 1 km. This is the area we interpret geologically in the main text.

Dependence of inversion on velocity model

Errors due to uncertainties in the velocity model can be estimated by repeating the inversions from the two "flat-Moho" starting models with different velocity models (figs. A2-4 and A2-5). Our "data" are the observed travel-times from the SSCD data, and so the best result of the inversion is our final model in figure 3b. For each starting interface, we chose a 1-D velocity model (velocities increasing linearly with depth) that generated reflection-times close to the observed times for some of the shots (SPs 1 and 5 were examined for this purpose).

Since there is a perfect trade-off between velocity and depth error only for data with a single angle of incidence (*Bube et al.*, 1995), the true reflector can still be partially

reconstructed. Because the observed curvature of the P_mP reflection hyperboloid depends on the crustal velocities, a match between modelled and observed times can only be achieved locally with wrong velocities. Therefore these data *do* provide constraints on Moho depth *as well as* velocities. Obviously, the velocity gradient in the Moho depth range (for the 1-D test velocity models the gradient is constant for the entire crust) is the most sensitive parameter for the inversion. The largest differences in A2-4c and A2-4d are consequently found where the test gradient is inappropriate: model A2-4b (difference plot A2-4d) has, in the Sierra Nevada, both too high average velocities (6.5 km s^{-1} vs. typically 6.1 km s^{-1} in our 3-D model) and too high a velocity gradient (0.022 s^{-1} vs. typically 0.017 s^{-1} in our 3-D model). Model A2-4a has an even higher velocity gradient (appropriate for the Great Valley basement) of 0.033 s^{-1}, but a low average velocity (6.0 km s^{-1}); the overall differences with our final model (A2-4c) are therefore smaller (the high values in the area $100 \leq X \leq 150$ are purely due to extrapolation into unconstrained areas; our final model tries to suppress these artifacts). Choosing a gradient and average velocity (0.017 s^{-1} and 6.1 km s^{-1}) that is appropriate for the Sierra Nevada reduces the differences there considerably (fig. A2-5)

Despite large deviations in the first two iterations of the inversions, after the third iteration, the interface has converged towards our final model within 3 to 10 km where our model is constrained. Note that the largest deviations (figs. A2-4c to e) occur between suites of reflection points of two or more shots at far offsets (between NPE and the refraction lines, between SPs 2 and 4, SPs 7 and 9, and SPs 4 and 19), i.e. the part most sensitive to wrong velocities, and where a low is created by extrapolation from reflection points on a steep slope (halfway between SPs 3 and 13).

Summary

We can now summarise typical errors arising from different problems in the inversion:

model A2-1:	depth error due to incorrect starting Moho model	≤ 1km
models A2-3:	depth error due to incorrect starting Moho model	≤ 1km
model A2-4a:	depth error due to incorrect velocity model and incorrect starting Moho model	≤ 6 km
model A2-4b:	depth error due to incorrect velocity model and incorrect starting Moho model	≤ 10 km
model A2-5:	depth error due to incorrect velocity model and incorrect starting Moho model	≤ 4 km

Our tests show that if we know the crustal velocity structure (figs. A2-1, A2-3) then the errors in our final Moho model are tiny, ≤ 1km. However, if we have essentially no knowledge of the crustal velocity structure (i.e., we ignore all the P_g information) then unsurprisingly our errors are much larger, in the range of 3 to 10 km depending on the starting model (fig. A2-4).

Note that inversion A2-4a came closer to the "true" Moho depth and average crustal velocity than inversion A2-4b, and that the errors in figure A2-4c are correspondingly lower than in figure A2-4d. The differences in figure A2-4c are smaller than 3 km where P_mP reflection points provide real constraints, and smaller than 6 km where the interface was extrapolated between reflection points from different shots. In figure A2-5b even the average difference is well below 4 km, and larger differences are only observed for the far-offset reflection points from shotpoint 11 (localised nothwest of SP 9), which sees higher lower-crustal velocities in the 3-D model. We expect that our errors in figure 3b will be even smaller, because in our real Moho inversion we used a 3-D velocity model derived from the P_g arrival times. Our 3-D model is clearly far superior to the 1-D model used in the test A2-4a because the 3-D model has an rms-

misfit of only 118 ms (table A2-1) whereas the 1-D model has an rms-misfit twenty times larger. Hence we expect the errors in our final model (fig. 3b) to be substantially smaller than those seen in the test, figure A2-4c, and we feel justified in our claim in the main text that the error in our model is only ±3 km.

Additional reference cited

Bube, K.P., Langan, R.T., and Resnick, J.R., 1995, Theoretical and numerical issues in the determination of reflector depths in seismic reflection tomography, Journal of Geophysical Research, v. 100, no. B7, p. 12449-12458

Table A2-1

Tomographic velocity inversion statistics

number of iterations	filter width X x Y x Z (km)	rms misfit (ms)
1D starting model		2574
9	200 x 200 x 8	392
6	100 x 100 x 4	346
10	60 x 60 x 2	273
17	40 x 40 x 2	197
5	40 x 40 x 2	201
5	20 x 20 x 2	142
4	10 x 10 x 2	132
2	5 x 5 x 2	118 (131 for P_n)

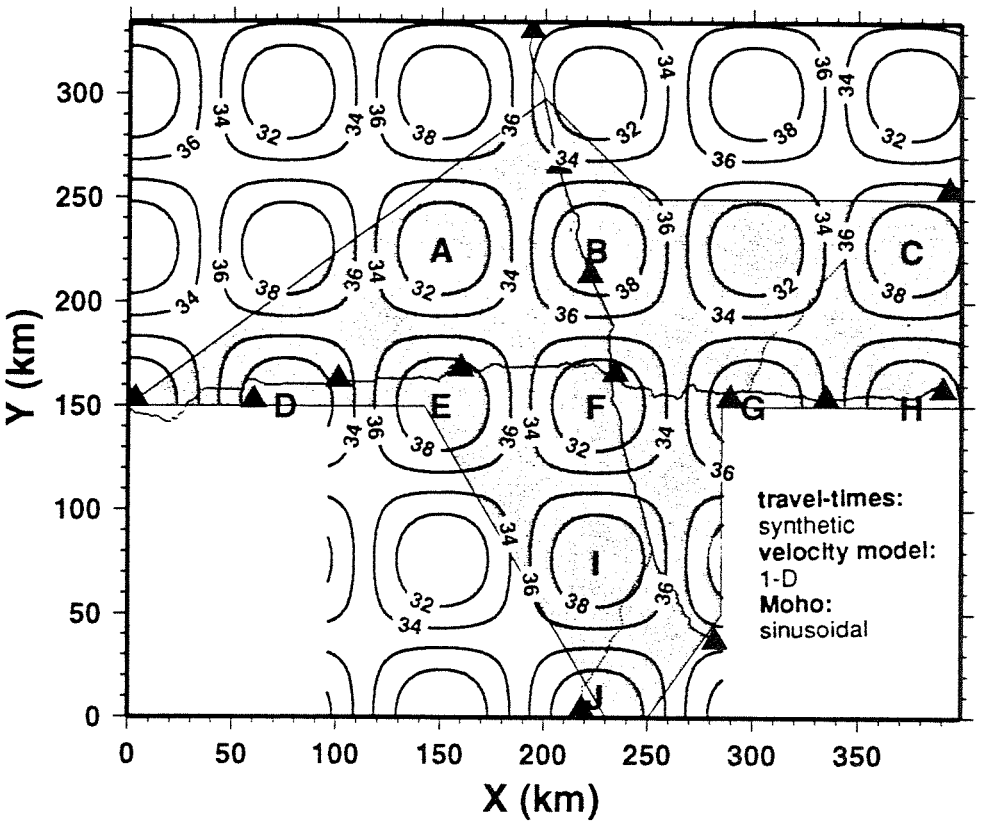

A2-1a Sinusoidal interface, for which synthetic travel-times were calculated; gray stippled area is area contoured in fig. 3b. Contours are Moho depths in km.

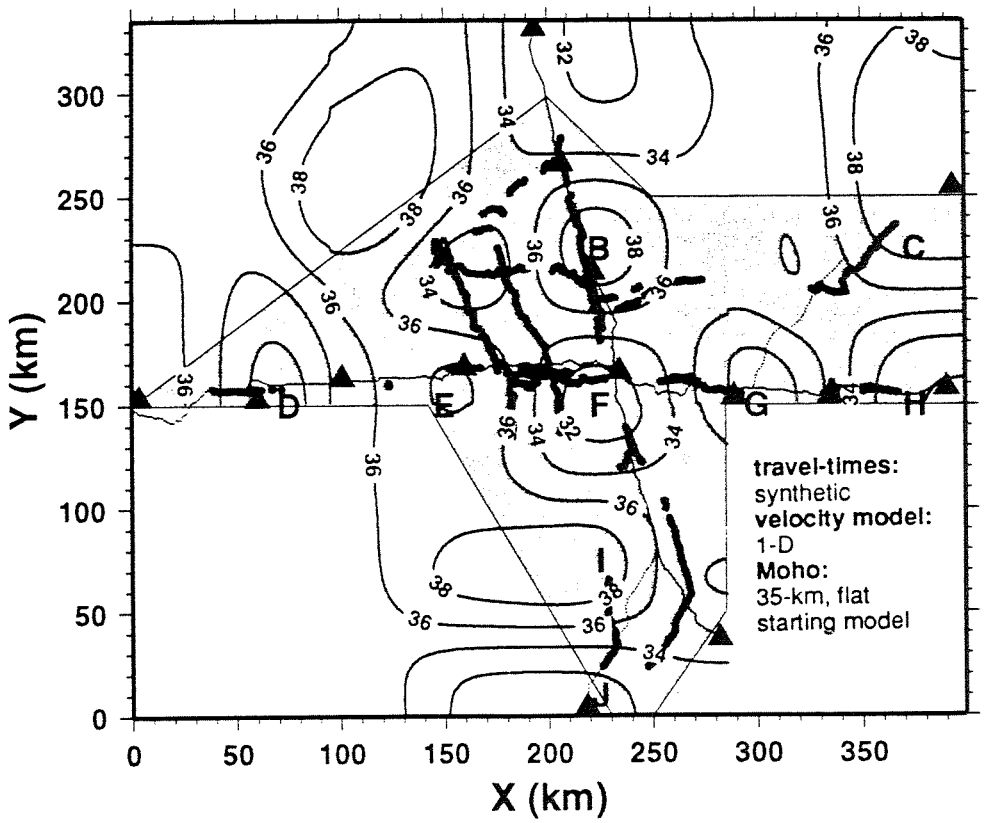

A2-1b Result after four iterations. In the first iteration rms-misfit with synthetic data was 2.2 km, in the second iteration 0.89 km, and in the third iteration 0.55 km. The final rms-misfit is 0.51 km for the points (black dots) from which Moho reflections are recorded.

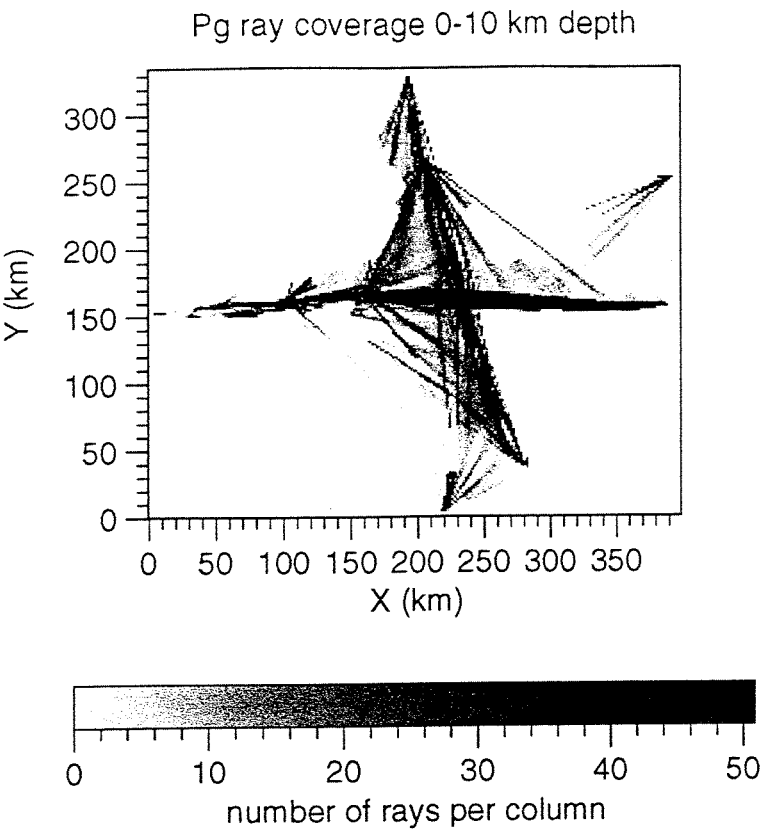

A2-2a P_g ray coverage integrated from 0 to 10 km depth in 1 km x 1 km columns

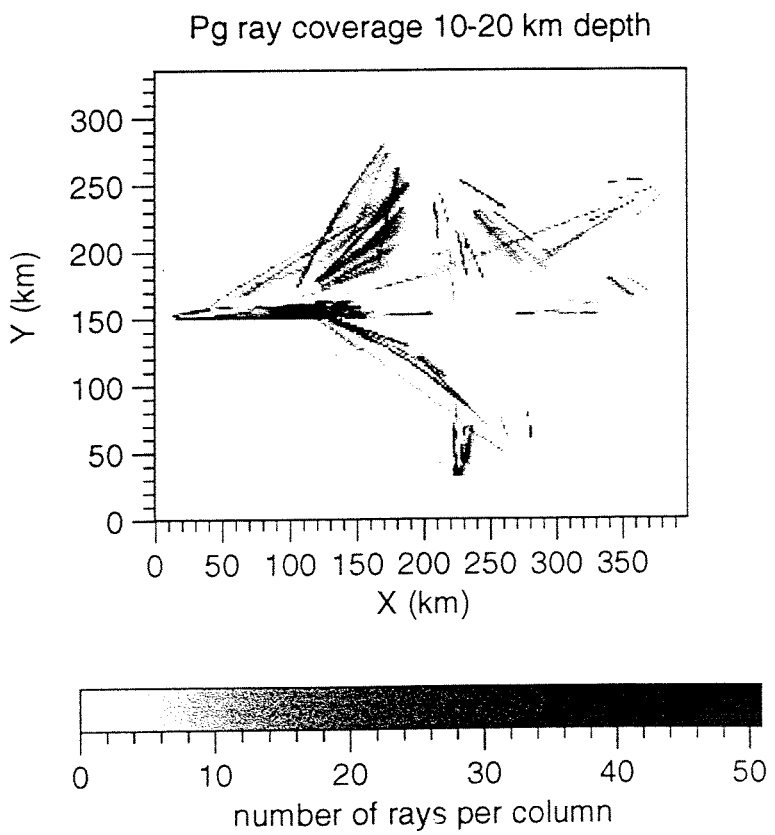

A2-2b P_g ray coverage integrated from 10 to 20 km depth in 1 km x 1 km columns

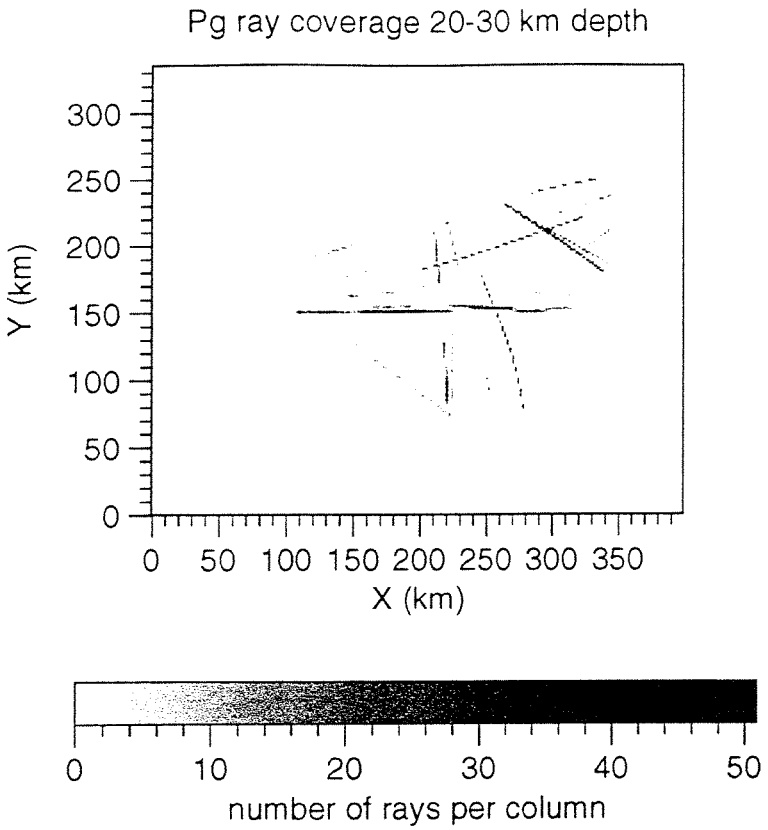

A2-2c P_g ray coverage integrated from 20 to 30 km depth in 1 km x 1 km columns

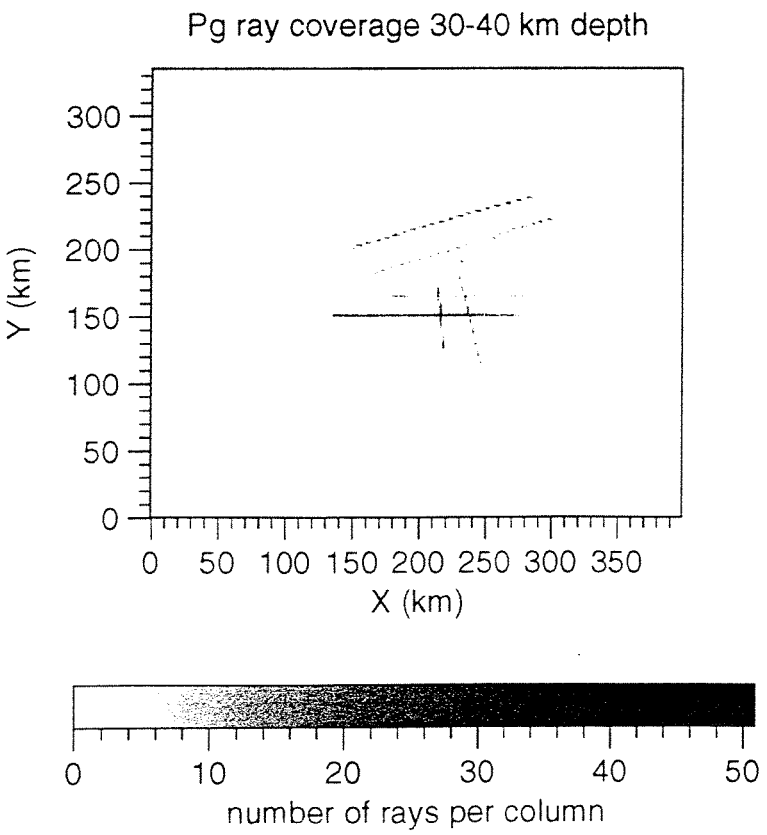

A2-2d P_g ray coverage integrated from 30 to 40 km depth in 1 km x 1 km columns

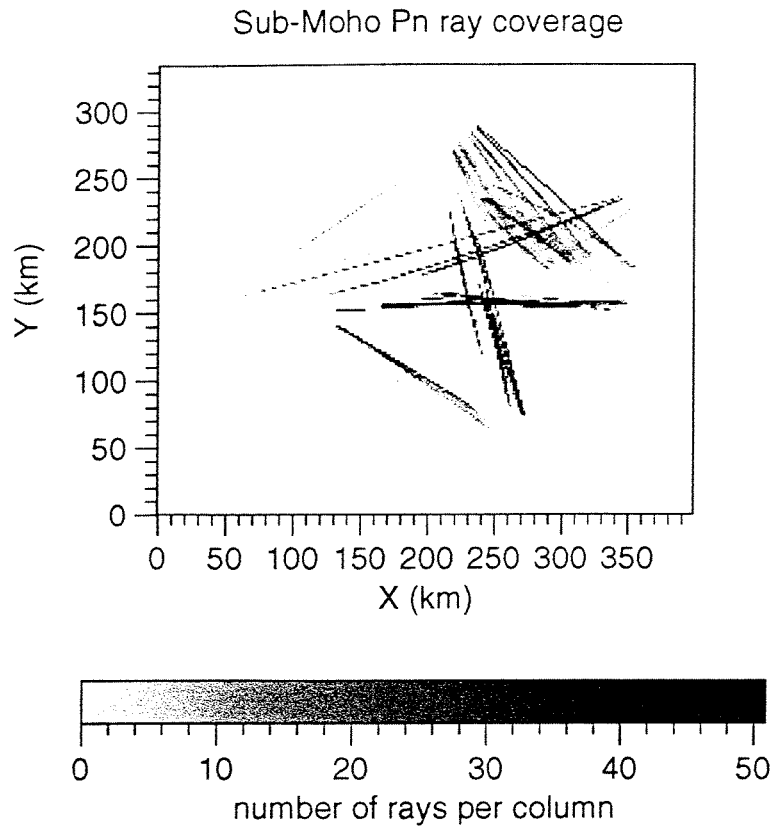

A2-2e P_n ray coverage integrated over all depths beneath the Moho in 1 km x 1 km columns

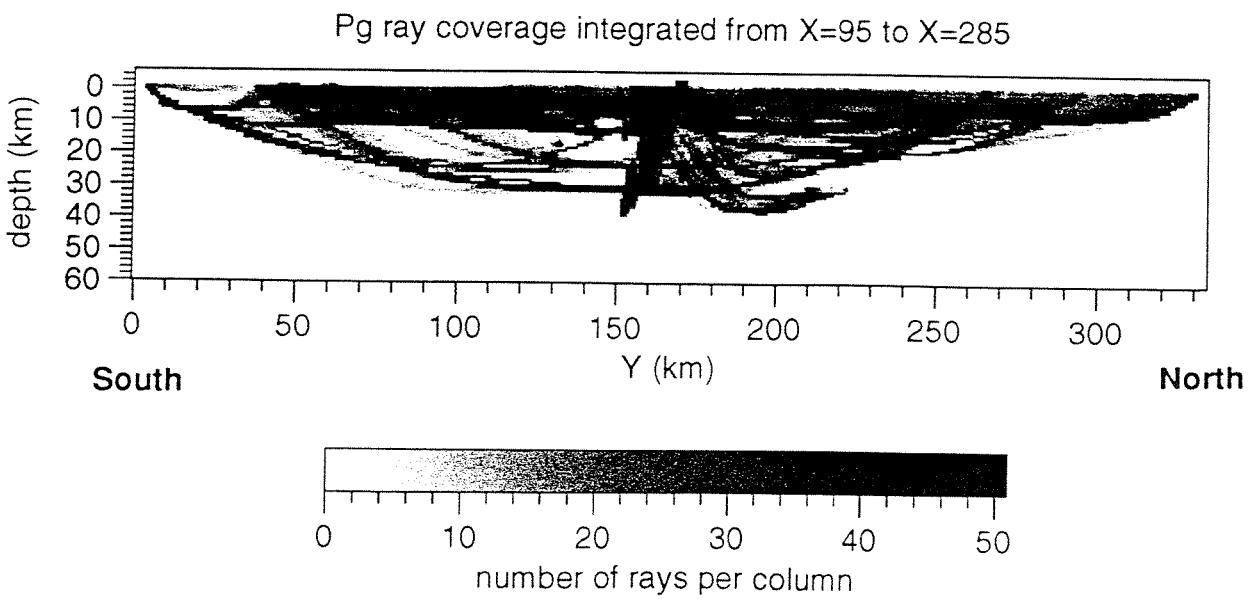

A2-2f P_g ray coverage in vertical south-north section

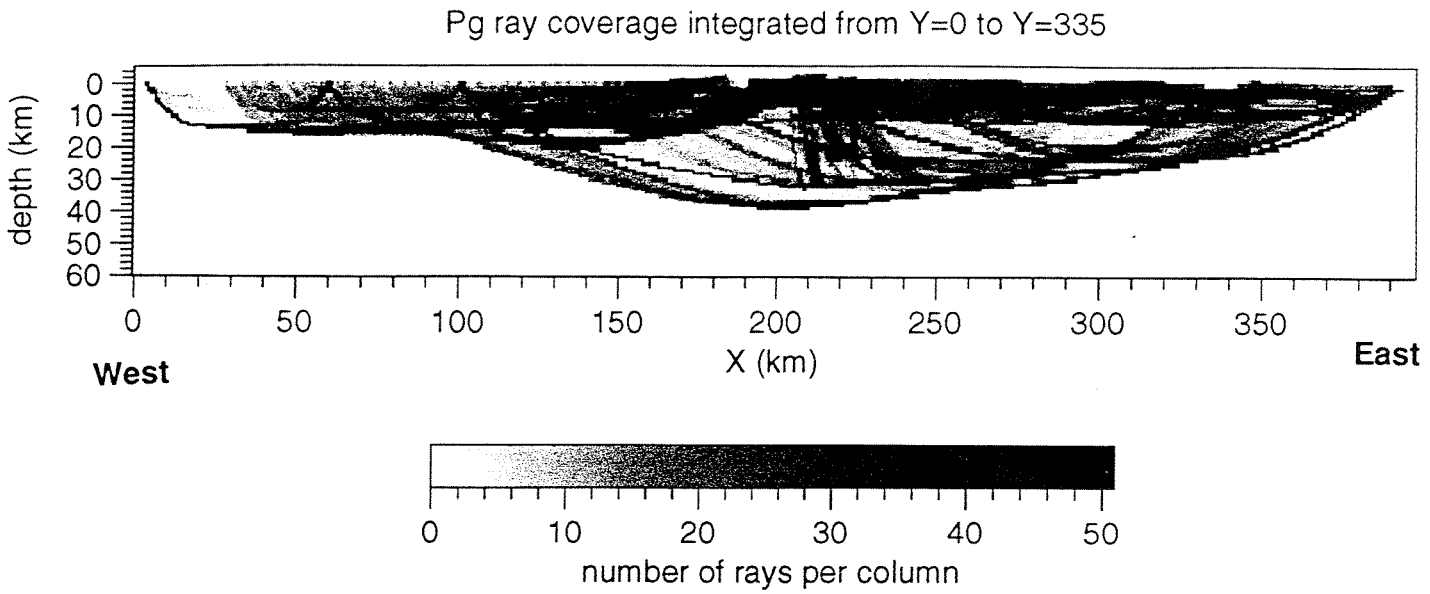

A2-2g P_g ray coverage in vertical west-east section

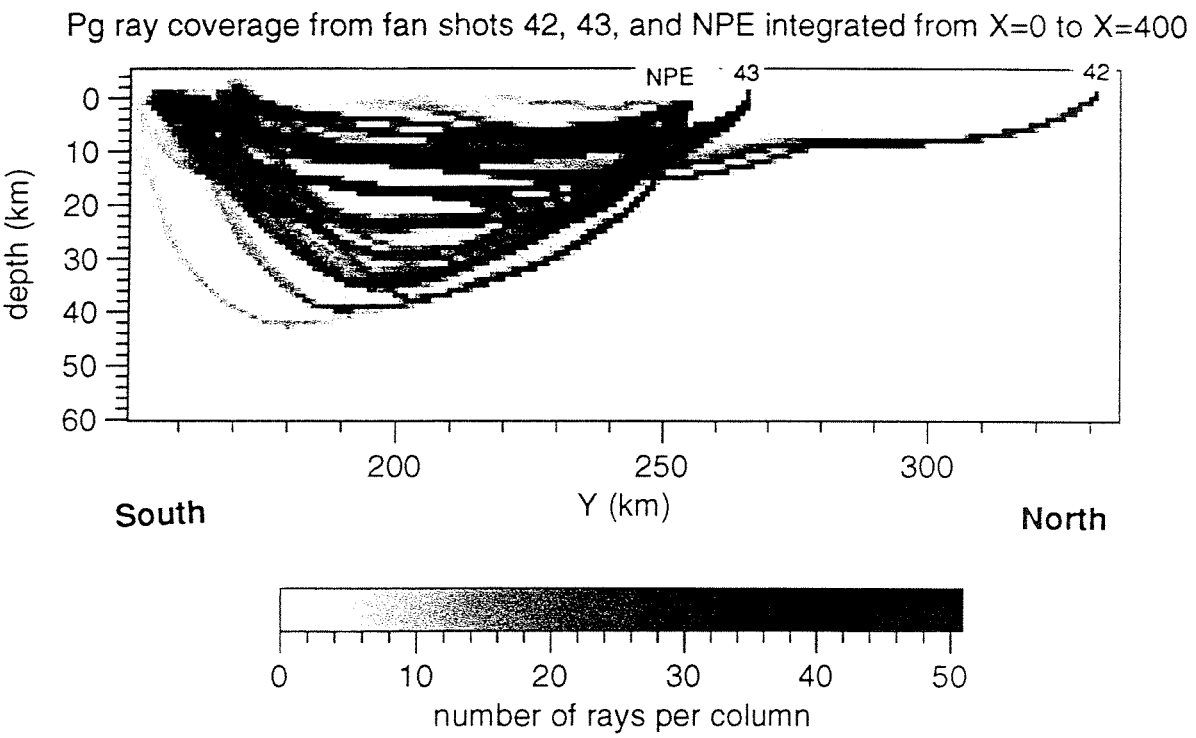

A2-2h P_g ray coverage in vertical south-north section provided by only three shots, SP 42, 43, and NPE.

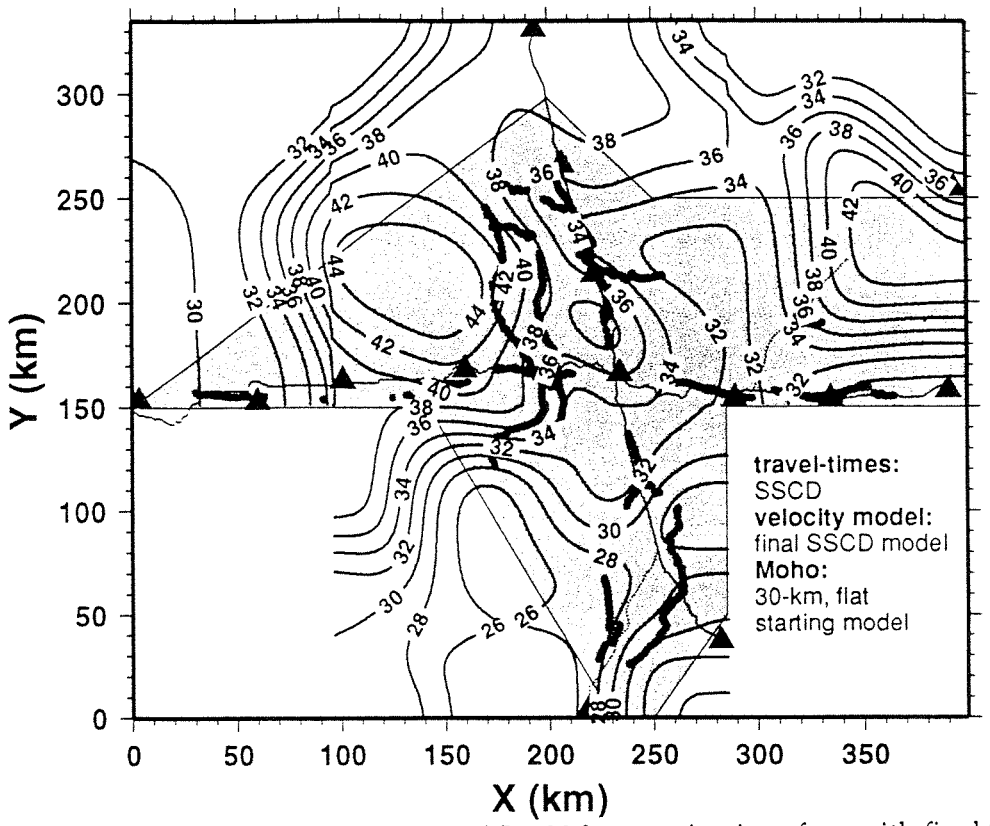

A2-3a Result after two iterations of flat 30-km starting interface with final 3-D velocity model (rms-misfit in the first iteration was 7.8 km, final rms-misfit is 2.3 km). Stippled area is the area contoured in figure 3b. Contours are Moho depths in km.

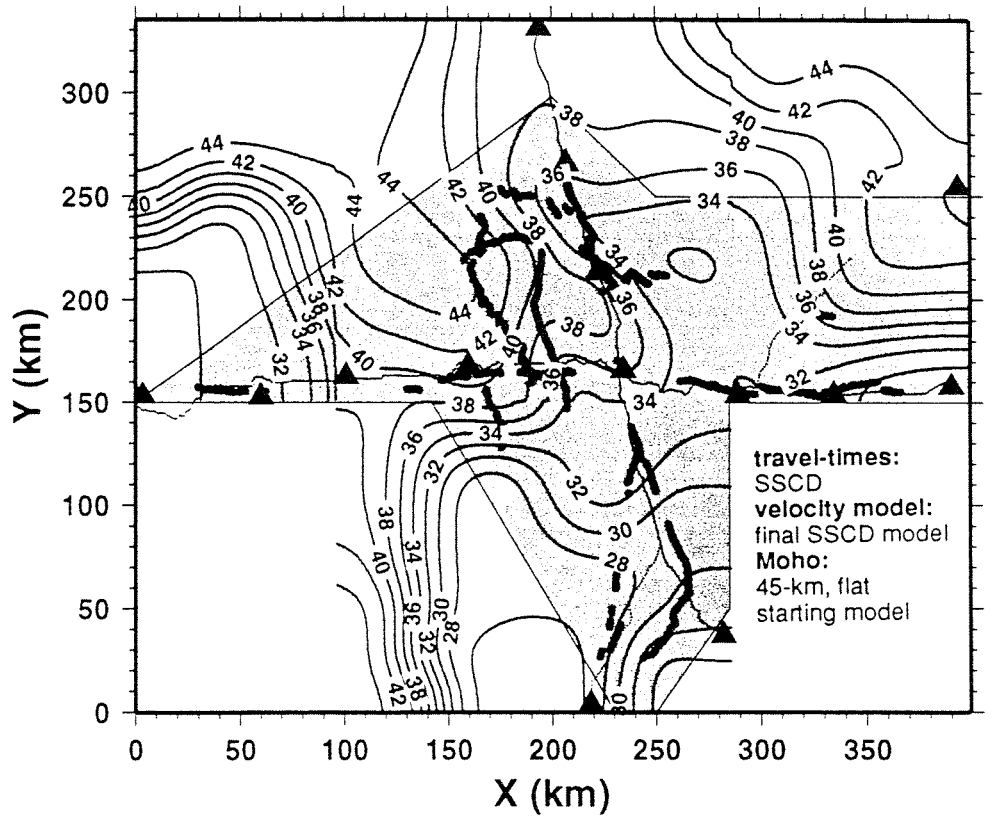

A2-3b Result after two iterations of flat 45-km starting interface with final 3-D velocity model (rms-misfit in first iteration was 9.7 km, final rms-misfit is 2.6 km)

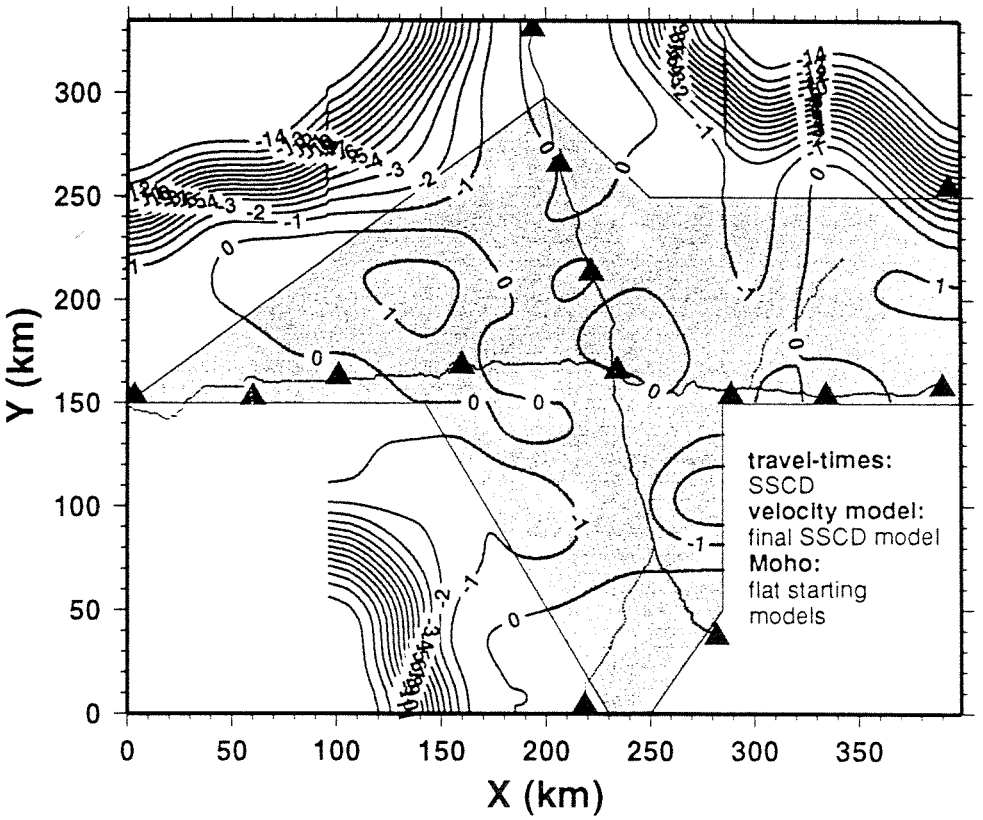

A2-3c Difference between A2-3a and A2-3b

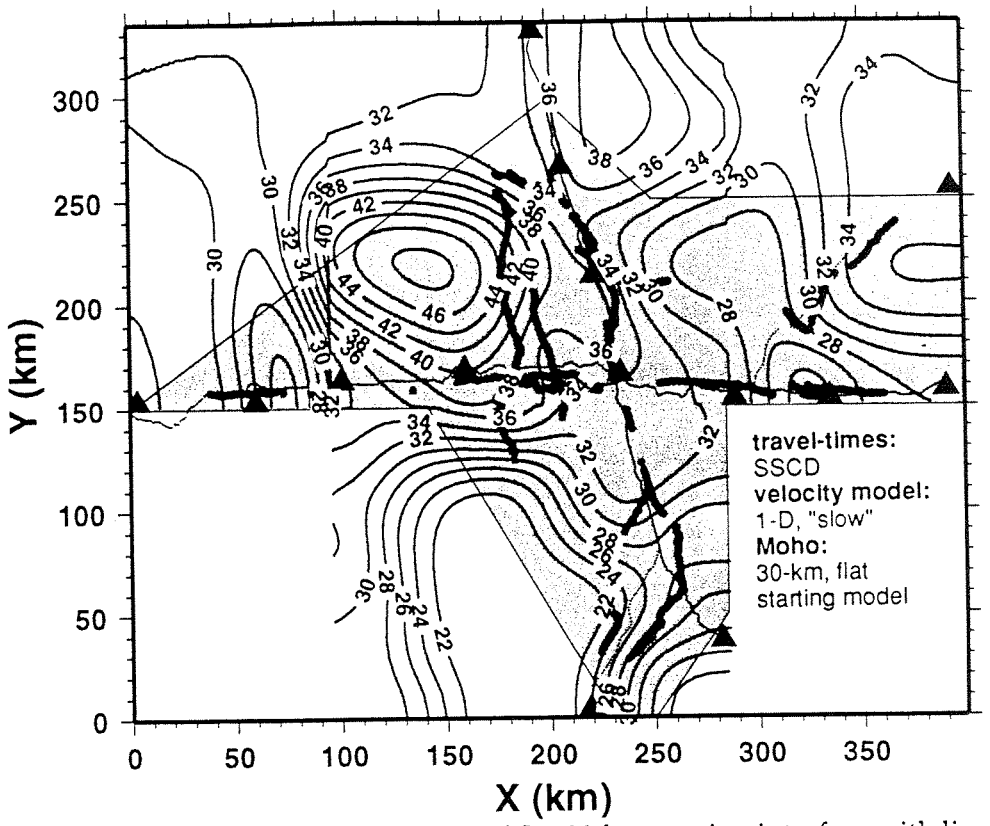

A2-4a Result after three iterations of flat 30-km starting interface with linear 1-D velocity model (surface velocity 5.5 km s^{-1}, velocity at 30 km depth 6.5 km s^{-1}, average velocity 6.0 km s^{-1}). In first iteration rms-misfit with data was 7.8 km, in second iteration 3.8 km; final rms-misfit is 2.7 km. Contours are Moho depths in km; black dots are reflection points.

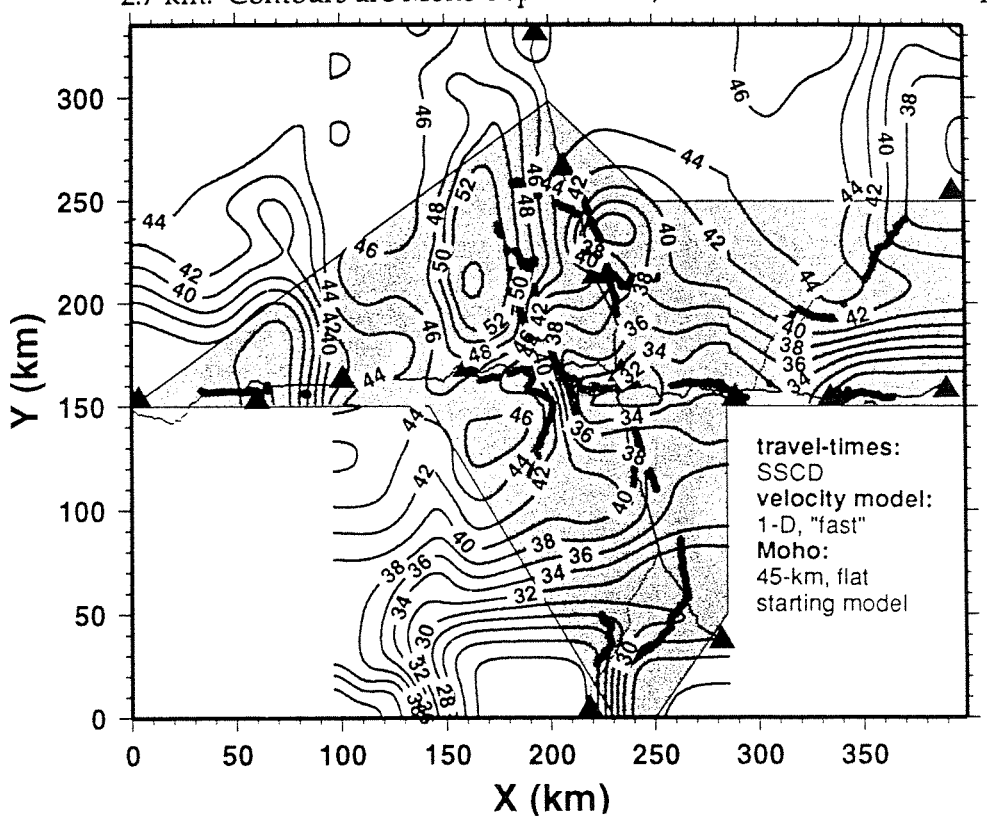

A2-4b Result after three iterations of flat 45-km starting interface with linear 1-D velocity model (surface velocity 5.5 km s^{-1}, velocity at 45 km depth 7.5 km s^{-1}, average velocity 6.5 km s^{-1}). In first iteration rms-misfit with data was 9.2 km, in second iteration 4.6 km; final rms-misfit is 2.9 km.

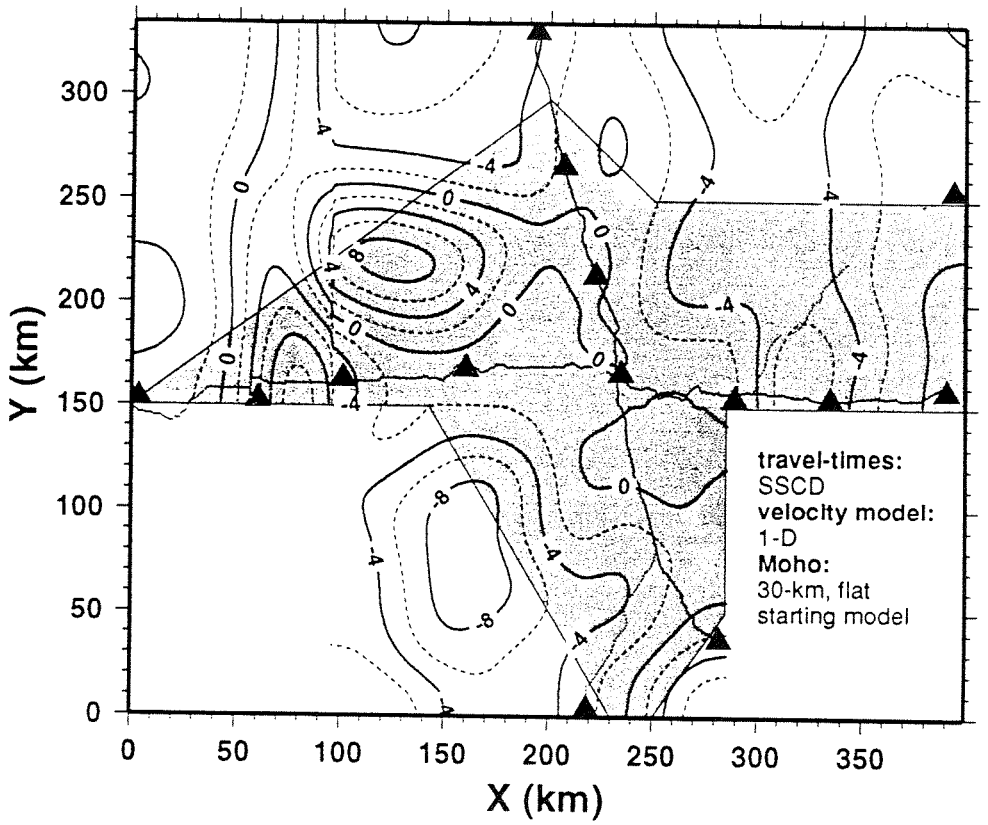

A2-4c Difference between A2-4a and our final Moho model

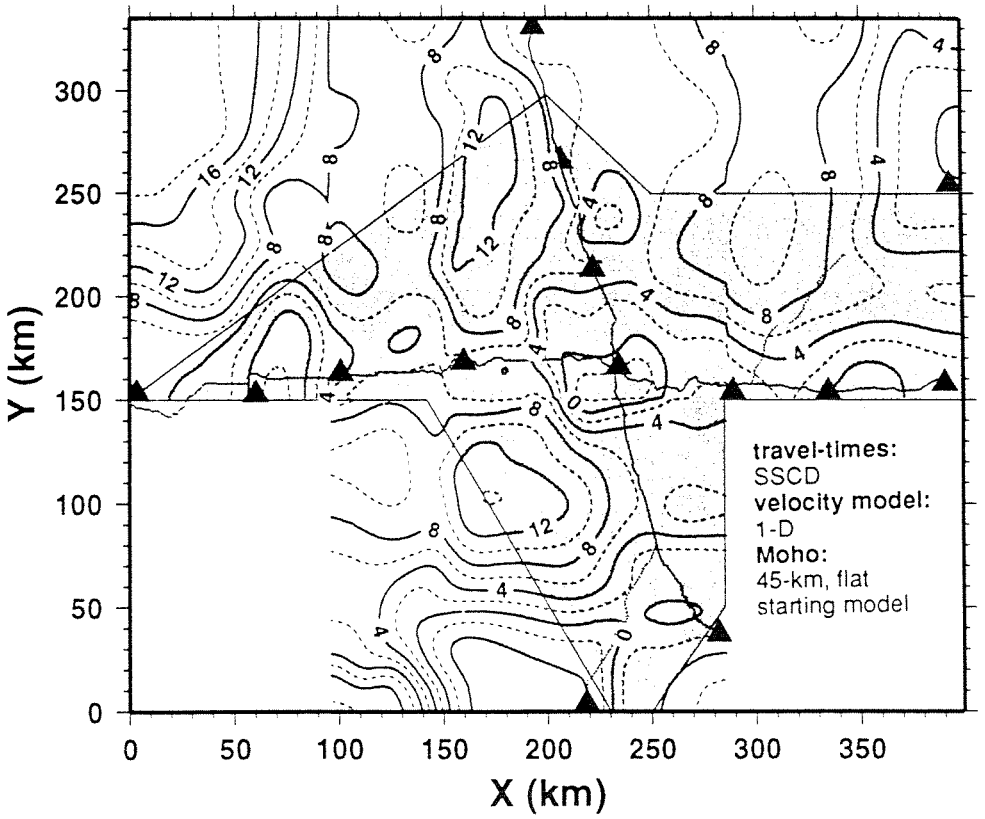

A2-4d Difference between A2-4b and our final Moho model

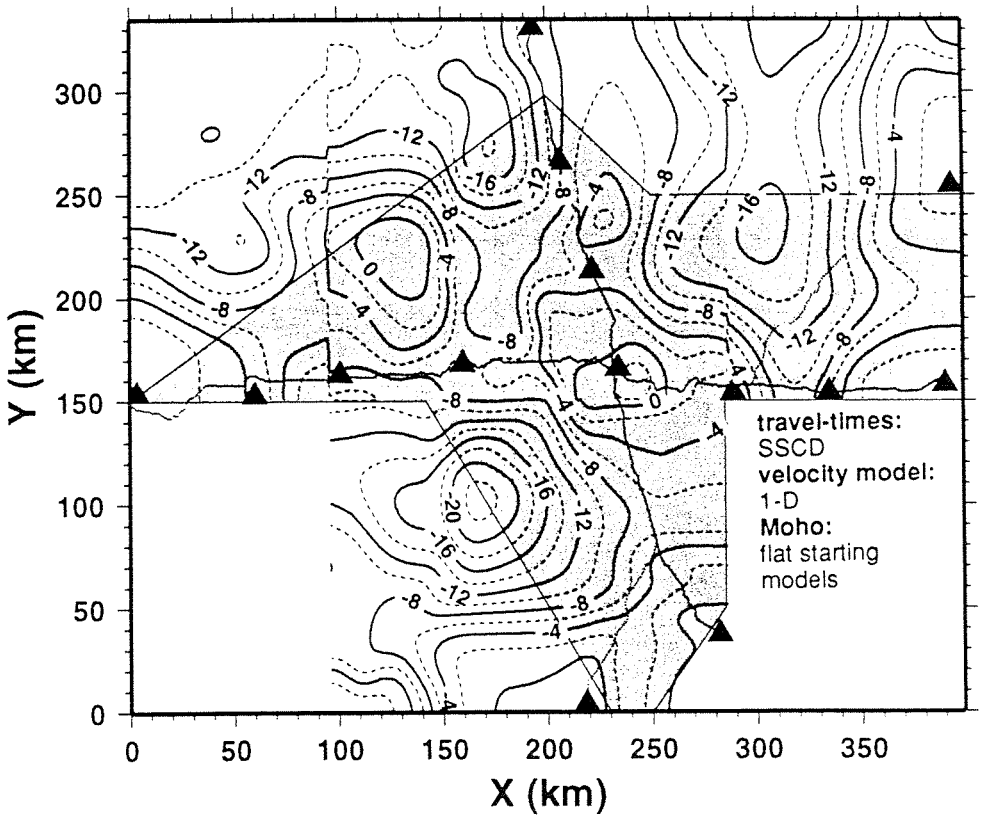

A2-4e Difference between A2-4a and A2-4b.

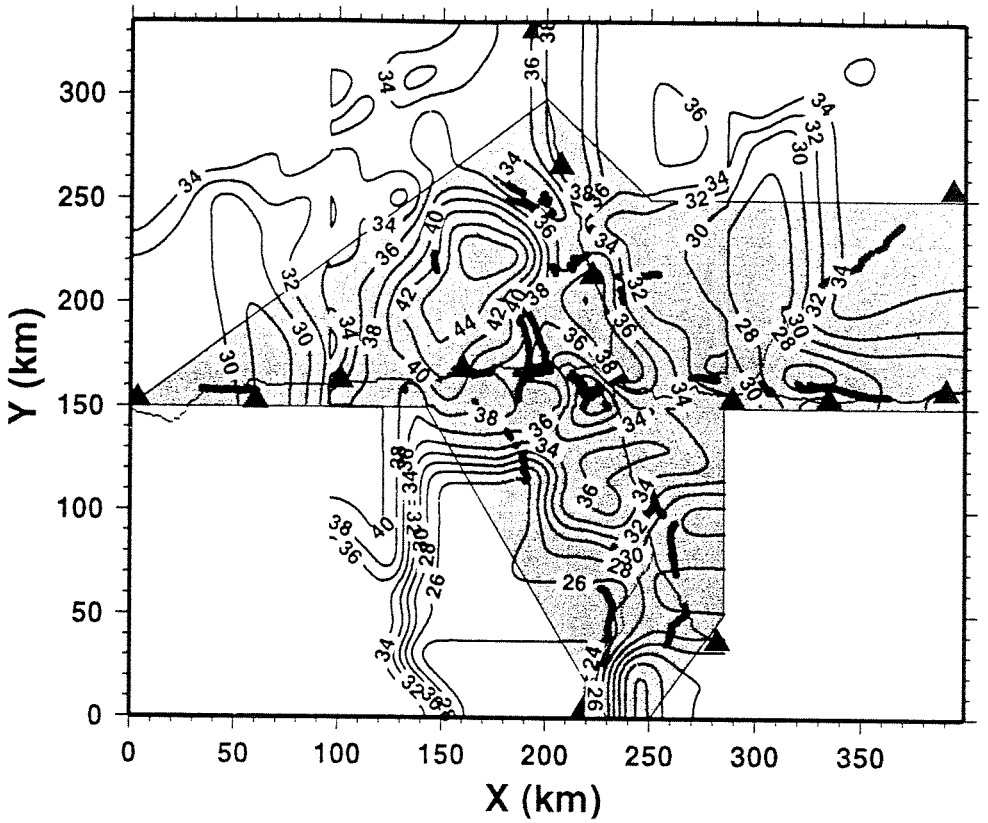

A2-5a Result after three iterations of flat 35-km starting interface with linear 1-D velocity model (surface velocity 5.8 km s^{-1}, velocity at 35 km depth 6.4 km s^{-1}, average velocity 6.1 km s^{-1}). In first iteration rms-misfit with data was 5.7 km, in second iteration 4.2 km; final rms-misfit is 2.5 km.

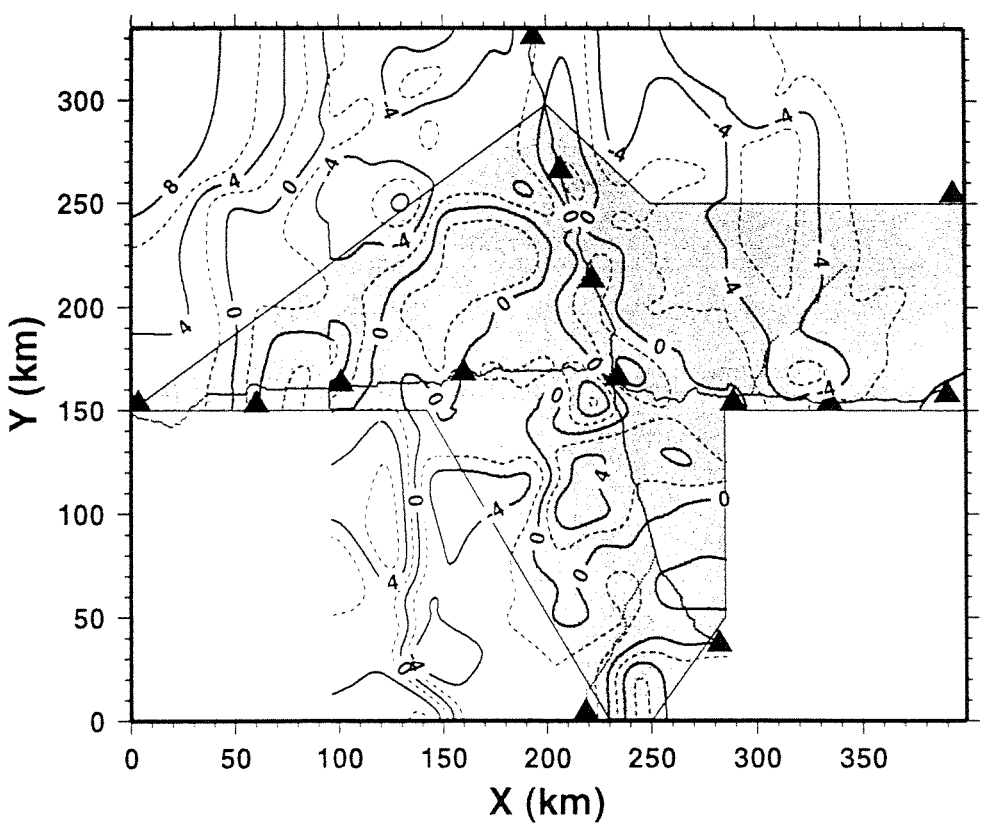

A2-5b Difference between A2-5a and our final Moho model.